J. Fluid Mech. (2024), *vol*. 999, A79, doi:10.1017/jfm.2024.960

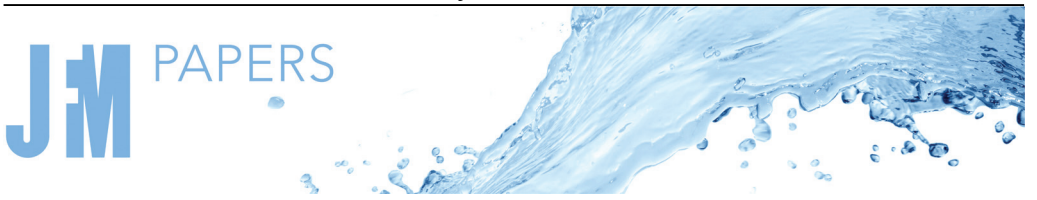

Curved detonation equations with analysis and its applications

Hao Yan[1], **Chongguang Shi**[1], **Haochen Xiong**[1], **Xin Han**[1] **and Yancheng You**[1],†

[1]School of Aerospace Engineering, Xiamen University, Xiamen, Fujian 361005, PR China

(Received 22 March 2024; revised 6 August 2024; accepted 28 September 2024)

In this paper, curved detonation equations with gradients for the pre-wave and post-wave are constructed followed by analysis, verification and applications. The study focuses on shock induced chemical reaction such as detonation, with the energy effect for the main attention. Equations consider both planar and transverse curvature to accommodate both planar and axisymmetric flow problems. Influence coefficients are derived and used to analyse the effect of energy and curvature on the post-wave gradient. Good agreement with the simulation results demonstrates that the equations presented in this paper can calculate various post-wave gradients accurately. After verification, the equations can be applied to applications, including not only solution and analysis but also in the inverse design. First, the method can be applied with polar analysis to provide a new perspective and higher order parameters for the study of detonation. Second, the equations can be used for the capture of detonation waves, where both planar and axisymmetric examples show better performance. Furthermore, the equations can be used in the inverse design of detonation waves in combination with the method of characteristics, which is one of the unique benefits of the present equations.

Key words: shock waves, detonations

1. Introduction

Shock waves are important phenomenon in supersonic flow and, therefore, shock-induced chemical reactions are of great interest, such as detonation and air dissociation. Detonation waves are supersonic combustion waves induced by shock waves and sustained by the subsequent chemical reactions (Teng & Jiang 2012). The early observations of detonation originated from mining disasters caused by the accumulation of coal-mine gas and explosions caused by gas leakage from chemical plants. The destructive ability of detonation is much greater than that of ordinary combustion phenomena, and thus

† Email address for correspondence: yancheng.you@xmu.edu.cn

it has attracted great attention. Abel (1874) first measured the detonation velocity of cotton powder. After this, Berthelot & Vieille (1881) systematically measured the detonation velocities produced by mixing various gaseous fuels with different oxidants. This systematic and comprehensive study confirmed the existence of the detonation wave. Since then, detonation has gradually developed into a discipline of experimental, theoretical and numerical investigations with its research category, governing equations and basic laws.

Due to the complexity of the detonation phenomenon, experimental testing has long been the main research method, especially in early studies. Many important physical phenomena have been elucidated through experimental observation. Chatelier (1885) recorded the evolution process from deflagration to detonation, and they confirmed for the first time that there can be two combustion modes in the same combustible gas: a deflagration wave and a detonation wave. Denisov (1959) experimentally observed the cell structure of a detonation wave. Theoretical approaches have also accompanied the development of detonation research. Using the Rankine–Hugoniot (RH) relations, Chapman (1899) and Jouguet (1904, 1905, 1916) established theories to analyse the conservation equation of crossing detonation waves, and they obtained the unique solution of the stable propagation velocity of a detonation wave, which is called the Chapman–Jouguet (CJ) velocity. CJ theory is a very important achievement, but it ignores the complex structures of detonation waves. To this end, Zel'dovich (1940), Von Neuman (1942) and Doring (1943) independently put forward a theoretical model to describe the detonation wave structure, which is referred to as the ZND model. The ZND model successfully combines the chemical reaction process and shock dynamics, establishing a complete theoretical detonation model with a clear concept that considers both physical and chemical phenomena. It thus makes a great contribution to the study of detonation. With the development of computer technology, Taki & Fujiwara (1978) successfully simulated an unsteady detonation wave for the first time and obtained the three-wave structure of the detonation wave. Eto, Tsuboi & Hayashi (2005) calculated the propagation of an explosion wave in a three-dimensional pipeline and found the law of three-wave points propagating along the diagonal. Dou *et al.* (2008) studied the propagation patterns of implosion waves in rectangular pipelines by using a fifth-order weighted essentially non-oscillatory scheme and the third-order total variation diminishing Runge–Kutta method.

In any real detonation, there will always be some curvature of the detonation wave, however small (Sharpe 2007*b*). Even a small amount of curvature can have a significant effect on the detonation wave structure (Klein & Stewart 1993; Yao & Stewart 1995). Hornung (1998) solved the inviscid equations of motion for the reacting flow at the downstream side of a curved shock for the shock-normal derivatives and explained the formation of the cellular structure by solving the post-wave streamline curvature. In terms of projectile-induced detonation, Maeda, Kasahara & Matsuo (2012) and Maeda *et al.* (2013) discussed detonation stability owing to the curvature effect arising from the three-dimensional nature of a stabilized oblique detonation wave around a projectile. Their previous studies showed that the detonation wave near the projectile was attenuated below the CJ velocity by the curvature effect (Menees *et al.* 1992; Kaneshige & Shepherd 1997). Regarding detonation behind a conical flow, Yang *et al.* (2017) performed further simulations to investigate the interplay between the effect of Taylor–Maccoll flow, front curvature and energy release from the chemical reaction in conical oblique detonations. Their simulations showed that the curvature can overcompensate for the high density and temperature in the shocked gas, which means that the curvature plays a more

dominant role in the initiation of conical oblique detonation. In the studies of Verreault, Higgins & Stowe (2012) and Verreault (2011), the presence of the curvature was found to allow oblique detonation waves to be initiated at an angle less than that of planar CJ oblique detonation. There have also been some one-dimensional studies, where Watt & Sharpe (2004) performed a one-dimensional study of the stability of weakly curved, quasi-steady detonation waves using a numerical shooting method. Their results show that even weak curvature has a significant destabilizing effect on detonation waves. Sharpe (2007*a*) determined the detonation speed–curvature relations for a small but non-zero front curvature and proposed that slightly curved detonation structures may be helpful for the understanding of cellular detonation.

It is worth noting that in the research of curved shock waves, Mölder (2016) proposed a curved shock theory in flows with planar or axial symmetry, which was applied to the relationships between pressure gradients, streamline curvature, vorticity and shock curvature. In a subsequent study, curved shock theory was used to calculate flow behind concave shock waves, and the analysis showed that shock curvature plays an important role in determining the flow properties behind double-curved shock waves (Mölder 2017*a*). In addition, curved shock theory has been applied to calculate flow near single and double curved shock waves, regular shock reflections, and Mach reflections on curved surfaces (Mölder 2017*b*). Curved shock theory has also been used to discover and demonstrate the effects of longitudinal and lateral wedge surface curvature on the detachment of shock waves from the leading edge of a double curved wedge tip (Mölder 2017*c*). These studies show that curved shock theory has an active role in the analysis of the flow, reflection and detachment of shock waves. Based on this theory, Shi *et al.* (2020) developed a second-order curved shock theory that is a re-derivation of the first-order derivative to obtain the second-order gradients. Further, a method of curved-shock characteristics based on curved shock theory was also constructed (Shi *et al.* 2021). Compared with the method of characteristics, the gradient information enhances the computational efficiency and accuracy of the method of curved-shock characteristics. Moreover, the curved shock theory can be extended to imperfect gases and unsteady flow (Emanuel 2018). Recently, curved shock theory has been developed to characterize the flow on the downstream side of a three-dimensional shock surface by Emanuel & Mölder (2022). This study extended the curved shock theory to three dimensions and enhanced its applicability even more. To summarize, on the one hand, curved shock theory can be employed for analyses such as flow after curved shock waves, shock reflections and detachment. On the other hand, curved shock theory can also be developed for unsteady, imperfect gases and three-dimensional curved shock waves. These opportunities demonstrate the significant research value and potential of the curved shock theory. In the meantime, inspired by the CJ theory and the ZND model, if the variations within the reaction zone are not required, a detonation wave can be considered as a reacting shock wave in which reactants transform into products and are accompanied by energy release.

For shocks with chemical reactions, it can be categorized into exothermic or endothermic depending on the specific chemical reaction. For example, detonation waves are generally induced by a shock to produce an exothermic chemical reaction. Combustible gases (e.g. hydrogen) undergoing shock will rise in temperature and pressure to reach combustion conditions, which will then initiate combustion. For example, hydrogen H_2 reacts with oxygen O_2 to form water H_2O. This process will release a large amount of energy and the chemical energy will be converted into heat energy, as shown in figure 1(*b*). Another classic endothermic reaction type is the air dissociation, where pure air will also increase in temperature and pressure after the shock, and, after reaching certain conditions

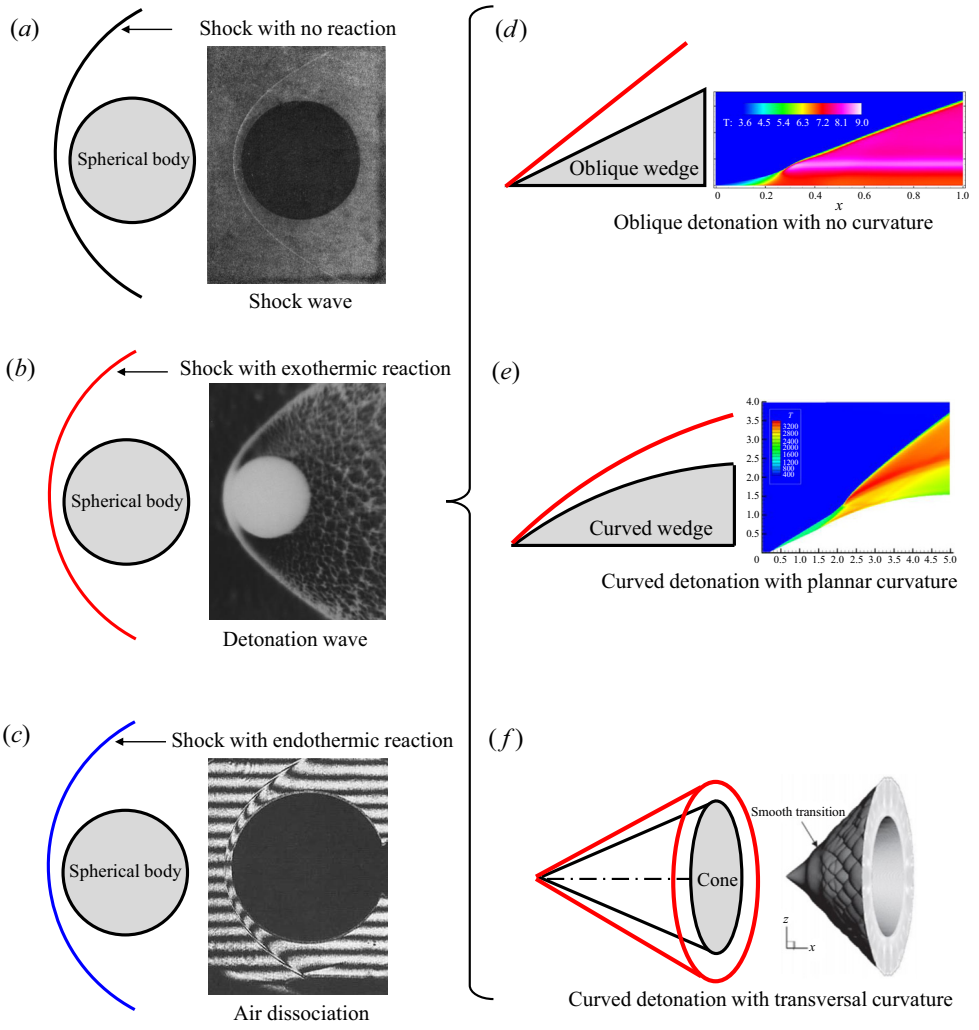

Figure 1. Schematic diagrams of curved shock waves with experimental or simulation results for reaction and no-reaction: (*a*) curved shock wave (Lobb 1964); (*b*) curved detonation wave (Kasahara *et al.* 2002); (*c*) curved dissociated air (Wen, Massimi & Shen 2017); (*d*) oblique detonation without curvature (Choi *et al.* 2007); (*e*) two-dimensional detonation with planar curvature (Xiang *et al.* 2022); (*f*) axisymmetric detonation with transverse curvature (Han, Wang & Law 2019).

(generally speaking, very high temperature), the air will dissociate. For example, the nitrogen molecule N_2 will dissociate into two nitrogen atoms and the oxygen molecule O_2 will dissociate into two oxygen atoms, and this process will absorb energy, as shown in figure 1(*c*). When the combustible gas or pure air does not reach the chemical reaction conditions, a shock wave will be formed, as shown in figure 1(*a*). However, according to the shape of the wave, more specifically the two curvatures in the planar and transverse directions, the wave can be classified into four types. Taking the detonation wave as an example, the first type is an oblique detonation wave without any curvature, as shown in figure 1(*d*), the second is a two-dimensional curved detonation wave with planar curvature, as shown in figure 1(*e*), the third is an axisymmetric detonation wave with transverse curvature, as shown in figure 1(*f*), and the fourth is a curved detonation wave

with curvatures in both directions, as shown in figure 1(*b*). To the best of the author's knowledge, there is no established theoretical method to systematically examine the effect of curvature in planar or conical reaction shock waves.

Inspired by the gas-dynamic theory of detonation, if the variations within the reaction zone are not required, the Rankine–Hugoniot relations are suitable for linking the upstream and downstream states across the wave (Lee 2008). In addition, Cheng, Luo & Dongen (2010) investigated the effect of heat addition on steady and unsteady flow in relation to condensation-induced waves. Apart from that, an instantaneous heat release CJ detonation model was considered to study the Mach reflection of the detonation wave by Bdzil & Short (2016). Inspired by these studies, a simplified reaction shock based on conservation laws is studied. The main difference between a reaction shock wave and no reaction shock wave in Rankine–Hugoniot relations is the energy release. To clearly elucidate the energy effect, we simplified the process of chemical reactions, as shown in figure 2. Here, τ_1 is located in front of the wave, τ_2 is located in the wave and τ_3 is just behind τ_2. The energy released from τ_1 to τ_2 is denoted as Q_d, and the energy released from τ_2 to τ_3 is recorded as Q_c. In other words, Q_d is the energy released when crossing the wave, while Q_c represents the energy released after the wave. Here, the wave can be a shock wave, as well as a dissociation or detonation wave. Therefore, it is worth clarifying again that the theoretical research in this paper is primarily for, but not limited to, detonation; it also applies to all shock-induced chemical reactions with an energy effect. As such, Q_d and Q_c can either be positive or negative and can also degenerate to zero. For example, when considering a detonation wave, Q_d is positive, while considering the dissociated air, Q_d is negative. In pathological detonations, Q_c has a negative value; in CJ detonations, Q_c is equal to zero; as for the other shock-induced combustion where the post-wave is a chemical non-equilibrium, Q_c is positive.

In recent decades, with the progress of detonation research and application, related numerical simulations and experimental observations have made great achievements. However, there are few breakthroughs in the theoretical study, so the CJ theory and ZND model are still the main representative works even though they were proposed decades ago. This greatly limits the profound understanding of detonation phenomena and hinders further applications. Therefore, an innovative breakthrough on theoretical research is urgently needed. Under such a motivation, considering the connection between shock and detonation waves, this paper supplements the energy effect on the basis of curved shock theory to make it applicable to detonation. By mathematical derivation in § 2, the curved detonation equations with energy effect are established and the relation between the pre- and post-wave gradients is developed. The influence coefficients are derived and subsequently used in the analysis of post-wave gradients in § 3. The verification is confirmed by a comparison with numerical simulation between the pressure gradients and the streamline curvatures in § 4. The results also suggest that the curved detonation equations can be a quick and effective method to forecast the post-wave gradients. Subsequently, the theory is applied in three aspects. First, polar curve analysis with gradients is proposed in § 5 to complement the previous polar analysis. Then the theory is applied to the capture of detonation waves in § 6, and by comparison with RH relations, the detonation wave captured through higher-order equations is more accurate. Finally, the theory can be used for the inverse design of detonation waves. The above analysis and applications show the unique benefits and potential value of the theoretical method proposed in this paper. Conclusions and future prospects are given in § 7.

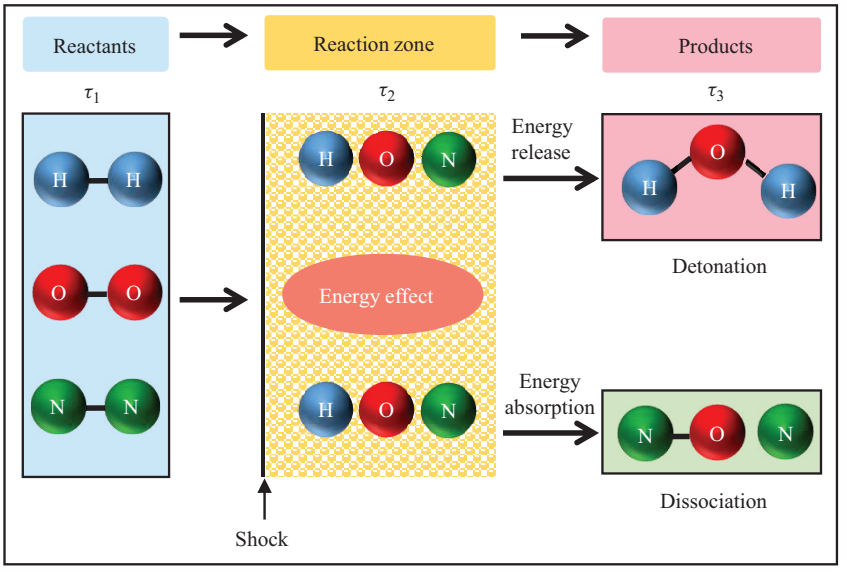

Figure 2. Simplified chemical reaction process in the shock-coupled chemical reaction, τ_1 is the reactants for the incoming flow, τ_2 represents the flow in the reaction zone and τ_3 indicates the products after the reaction wave.

2. Curved shock theory supplemented by energy effect

2.1. *Derivation of curved shock theory supplemented by energy effect*

A curved shock theory supplemented by the energy effect is determined in this section. The energy effects are mainly reflected in two aspects, one is the energy released/absorbed when crossing the shock and another part is the energy change following the shock.

2.1.1. *Rankine–Hugoniot equations with energy effect*

From figure 2, it is clear that the energy release Q_d will affect the Rankine–Hugoniot equations. As such, to describe the relationship between the airflow parameters before and after the curved detonation wave, a simplified curved detonation wave is shown in figure 3. Here, V_1 is the incoming velocity vector and V_2 is the leaving velocity vector. The flow-deflection angle δ is equal to the difference between the two angles of velocity to the x-axis, that is, $\delta = \delta_2 - \delta_1$. The length measured along the detonation wave is σ, and this can be decomposed into the sum of two vectors s and n, which are the length measured tangential and normal to the streamline, respectively. The detonation angle θ is defined as the angular difference between σ and V_1. The planar curvature S_a is denoted by the radius of curvature R_a, which means that $S_a = -1/R_a = \partial\theta_1/\partial\sigma$. By the same token, the transversal curvature S_b is represented by $S_b = -1/R_b = -\cos\theta_1/y$, where y is the distance from the detonation to the x-axis. According to the parameters and assumptions given above, the basic Rankine–Hugoniot equations of a curved detonation wave can be derived as

$$\left.\begin{aligned} \rho_1 V_{1n} &= \rho_2 V_{2n}, \\ p_1 + \rho_1 {V_{1n}}^2 &= p_2 + \rho_2 {V_{2n}}^2, \\ \frac{\gamma_1}{\gamma_1 - 1}\frac{p_1}{\rho_1} + \frac{V_{1n}^2}{2} + Q_d &= \frac{\gamma_2}{\gamma_2 - 1}\frac{p_2}{\rho_2} + \frac{V_{2n}^2}{2}, \end{aligned}\right\} \tag{2.1}$$

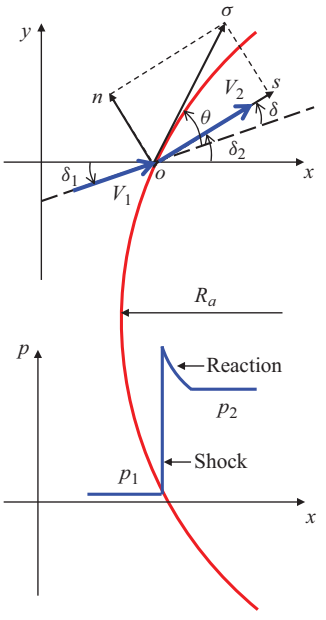

Figure 3. Curved detonation wave with airflow parameters in planar flow, velocity and pressure change in airflow through the curved detonation wave. Curvature S_a is expressed as the radius of curvature R_a, $S_a = -1/R_a = \partial\theta_1/\partial\sigma$, $\theta_1 = \theta + \delta_1$. Here, p_1 is the pre-wave pressure and p_2 is the post-wave pressure in detonation.

where ρ is the density, p is the pressure, V_n is the normal velocity and γ is the specific heat ratio. Subscripts 1 and 2 denote pre-wave and post-wave, respectively. Additionally, the chemical reaction can be calculated by a single-step Arrhenius reaction:

$$\bar{\omega} = k(1 - Z)\exp(-Ea/RT), \tag{2.2}$$

where $\bar{\omega}$ is the chemical reaction rate, k is the prefactor, Z is the chemical reaction process, Ea is the activation energy of the chemical reaction, and R and T are the gas constants and temperature, respectively. The energy release through the chemical reaction can thus be calculated as

$$Q_d = Q_0(Z_1 - Z_2), \tag{2.3}$$

where Q_0 is the total energy released when the chemical reaction is completed. In the single-step chemical reaction model, Z_1 and Z_2 denote the pre-wave and post-wave chemical reaction processes, respectively. Here, $Z_1 = 1$ for pre-wave, and Z_2 can obtain different values according to different chemical reaction progresses and it will be 0 when the reaction is completed. Based on (2.1), a formula for the post-wave parameters can be derived, which is given in Appendix A. To validate the formulation given in this paper, a comparative example is presented. In this paper, the post-wave parameters are first calculated by the ZND theory. After that, the energy released during the detonation can also be calculated. In this way, the post-wave parameters can be solved according to the derivation in Appendix A. The calculation results obtained by the two methods are compared in table 1, and it is easy to find that the post-wave parameters calculated by the RH relations with energy release are very close to the results obtained by the ZND model, so the post-wave parameters calculated in this paper are considered to be credible. The advantage of the present RH relations with energy release over the ZND model is that the

	p_2 (atm)	T_2 (K)	u_2 (m s^{-1})
ZND solution	39.861	3426.4	646
RH equations	39.493	3485.6	663
Error	0.92 %	1.7 %	2.6 %

Table 1. Comparison of post-wave parameters calculated through ZND solution (Zhang *et al.* 2022) and RH equations with energy release. The hydrogen–air mixture is $0.42H_2$+$0.21O_2$+$0.79N_2$ (equivalent ratio is 1), and the pre-wave temperature $T_1 = 300$ K, $p_1 = 1$ atm, $u_1 = 2500$ m s^{-1}. The ZND structure is calculated by the 9-species 19-reaction by the Jachimowski (1988) mechanism.

relatively accurate post-wave parameters can be acquired without considering the complex chemical reaction, but instead by only solving the aerodynamic equations. Moreover, the relationship between each parameter is expressed as a relatively simple explicit form, which greatly simplifies the difficulty of the detonation solution and helps to enhance the understanding of the aerodynamic relationship of the detonation.

2.1.2. *Euler equations with energy effect*

Something else that will be affected by energy release is the post-wave governing equations. Here, the Euler equations with energy release Q_c will be introduced. In contrast to shock waves, the Euler equations with energy release in the natural or intrinsic streamline coordinates are used as the governing equations for steady planar or axial flow in the following form:

$$\left.\begin{aligned} \frac{\partial}{\partial s}\rho V y^j + \rho V y^j \frac{\partial \delta}{\partial n} &= 0, \\ \rho V \frac{\partial V}{\partial s} + \frac{\partial p}{\partial s} &= 0, \\ \rho V^2 \frac{\partial \delta}{\partial s} + \frac{\partial p}{\partial n} &= 0, \\ \frac{\partial h}{\partial s} + V\frac{\partial V}{\partial s} + \frac{\partial Q_c}{\partial s} &= 0, \\ \frac{\partial h}{\partial n} + V\frac{\partial V}{\partial n} + \frac{\partial Q_c}{\partial n} &= 0, \end{aligned}\right\} \tag{2.4}$$

where j is 0 or 1 for planar or axial flow. To simplify the subsequent calculation and keep the form neat, curved shock theory defines the following variable gradients:

$$P = \frac{1}{\rho V^2}\frac{\partial p}{\partial s}, \quad D = \frac{\partial \sigma}{\partial s}, \quad \Gamma = \frac{\omega}{V}, \quad \omega = V\frac{\partial \sigma}{\partial s} - \frac{\partial V}{\partial n}, \tag{2.5a–d}$$

where P is the normalized pressure gradient, D is the streamline curvature, ω is the vorticity and Γ is the normalized vorticity. To simplify the influence brought about by the energy release, we also define the following three mathematical coefficients:

$$H = \frac{1-\rho(\gamma-1)Q_c/V}{1-\rho^2(\gamma-1)Q_cV/\gamma p}, \quad N = \frac{V-(\gamma-1)\rho Q_c}{V-(\gamma-1)\rho M^2 Q_c}, \quad J = \frac{V+\rho Q_c}{V-(\gamma-1)\rho M^2 Q_c}. \tag{2.6a–c}$$

With the help of these mathematical symbols, we can rewrite (2.4) in the following form:

$$\left.\begin{aligned} \frac{\partial \delta}{\partial n} &= -(HM^2-1)P - j\frac{\sin\delta}{y}, \\ \frac{1}{V}\frac{\partial V}{\partial s} &= -\frac{1}{\rho V^2}\frac{\partial p}{\partial s} = -P, \\ \frac{1}{\rho V^2}\frac{\partial p}{\partial n} &= -\frac{\partial \delta}{\partial s} = -D, \\ \frac{1}{\rho}\frac{\partial \rho}{\partial s} &= HM^2 P, \\ \frac{1}{\rho}\frac{\partial \rho}{\partial n} &= -M^2[ND + (\gamma-1)J\Gamma], \\ \frac{1}{V}\frac{\partial V}{\partial n} &= D - \Gamma. \end{aligned}\right\} \tag{2.7}$$

The detailed derivation process for these equations is shown in Appendix B. It should be explained here that when the energy release Q_c is 0, the three coefficients H, N and J will become 1, so the above equations are consistent with curved shock theory.

2.1.3. *Curved shock theory supplemented by energy effect*

As described in the previous section, the Rankine–Hugoniot equations can provide the relationship between the zero-order parameters. To further acquire the relationship between first-order gradients for the pre- and post-wave, the partial derivatives of the following equations need to be derived separately:

$$\left.\begin{aligned} \rho_1 V_1 \sin\theta &= \rho_2 V_2 \sin(\theta-\delta), \\ p_1 + \rho_1 V_1^2 \sin^2\theta &= p_2 + \rho_2 V_2^2 \sin^2(\theta-\delta), \\ V_1 \cos\theta &= V_2 \cos(\theta-\delta). \end{aligned}\right\} \tag{2.8}$$

For simplicity, only some of the critical derivation steps are shown here, and the complete derivation can be found in Appendix B. The basic derivation process is as follows: first, both sides of the conservation equation (2.8) are simultaneously derived with respect to σ; after this, the partial derivatives are decomposed into two derivatives tangential and normal to the streamline, $\partial\bullet/\partial s$ and $\partial\bullet/\partial n$:

$$\left.\begin{aligned} \left(\frac{\partial \bullet}{\partial \sigma}\right)_1 &= \left(\frac{\partial \bullet}{\partial s}\right)_1 \cos\theta + \left(\frac{\partial \bullet}{\partial n}\right)_1 \sin\theta, \\ \left(\frac{\partial \bullet}{\partial \sigma}\right)_2 &= \left(\frac{\partial \bullet}{\partial s}\right)_2 \cos(\theta-\delta) + \left(\frac{\partial \bullet}{\partial n}\right)_2 \sin(\theta-\delta), \end{aligned}\right\} \tag{2.9}$$

where $\bullet$ is a notation for generalized parameters, and the subscripts 1 and 2 represent the pre- and post-wave, respectively. Subsequently, after simplifying and organizing, the

curved shock theory supplemented by the energy effect can be obtained as follows:

$$\left.\begin{aligned} A_1P_1 + B_1D_1 + E_1\Gamma_1 &= A_2P_2 + B_2D_2 + E_2\Gamma_2 + CS_a + GS_b, \\ A_1'P_1 + B_1'D_1 + E_1'\Gamma_1 &= A_2'P_2 + B_2'D_2 + E_2'\Gamma_2 + C'S_a + G'S_b, \\ A_1''P_1 + B_1''D_1 + E_1''\Gamma_1 &= A_2''P_2 + B_2''D_2 + E_2''\Gamma_2 + C''S_a + G''S_b. \end{aligned}\right\} \tag{2.10}$$

For convenience, these equations are named curved detonation equations (CDEs). It is necessary to point out that the curved detonation equations derived in this paper are complete three equations rather than the two equations form of the curved shock theory, this is because the post-wave vorticity may be an important gradient and not eliminated. It should be noted additionally that the study in this paper only works for equilibrium flows and does not apply to unsteady flows. The coefficients of the pre-wave A_1, B_1 and E_1; A_1', B_1' and E_1'; and A_1'', B_1'' and E_1'' and the curvatures C and G; C' and G'; and C'' and G'' are completely consistent with curved-shock theory, so only the post-wave coefficients affected by energy release are listed in this paper:

$$\left.\begin{aligned} A_2 &= \sin\theta\cos(\theta-\delta)(2H_2M_2^2-2), \\ A_2' &= \sin\theta\cos\theta/\sin(\theta-\delta) + \sin\theta\cos\theta(3H_2M_2^2-4)\sin(\theta-\delta), \\ A_2'' &= (H_2M_2^2-1)\sin(\theta-\delta)\tan(\theta-\delta) + \cos(\theta-\delta), \\ B_2 &= \sin\theta(1-N_2M_2^2)\sin(\theta-\delta) - \sin\theta\cos^2(\theta-\delta)/\sin(\theta-\delta), \\ B_2' &= [\sin\theta\cos\theta(-1-N_2M_2^2\sin^2(\theta-\delta) \\ &\quad + 2\sin^2(\theta-\delta) - 2\cos^2(\theta-\delta))]/\cos(\theta-\delta), \\ B_2'' &= -2\sin(\theta-\delta), \\ E_2 &= -\sin\theta\sin(\theta-\delta)((\gamma-1)J_2M_2^2+1), \\ E_2'' &= \sin(\theta-\delta), \\ E_2' &= -\sin\theta\cos\theta\sin^2(\theta-\delta)((\gamma-1)J_2M_2^2+2)/\cos(\theta-\delta). \end{aligned}\right\} \tag{2.11}$$

From (2.10) and (2.11), the relationships between the first-order gradients among incoming flow conditions, energy release, curvatures and post-wave parameters are constructed. There are eight variables in the equations: P_1, D_1, Γ_1, P_2, D_2, Γ_2, S_a and S_b. As long as five of these are known, the remaining three can be solved by the curved-detonation equations. These equations can be used in the following ways. On the one hand, the post-wave gradients can be solved according to the pre-wave gradients, curvature and energy release, as described in § 4. On the other hand, we can also compute the curvatures according to the pre- and post-wave gradients with the energy release; this could be used in the capture and reverse design of a detonation wave as shown in § 6.

The above derivation process is mainly based on the assumption of instantaneous energy release, which is reasonable for a preliminary study. However, the absence of chemical reaction makes the study incomplete. To cover this weakness, we give the curved detonation equations with chemical reaction (single-step Arrhenius equation) in Appendix C. For convenience, curved detonation equations with chemical reaction are called CDEC to distinguish it from CDE. The relationship between CDEC and CDE can be illustrated from both qualitative and quantitative perspectives. Qualitatively speaking, when the chemical reaction related variables can be neglected, it is reasonable to simplify

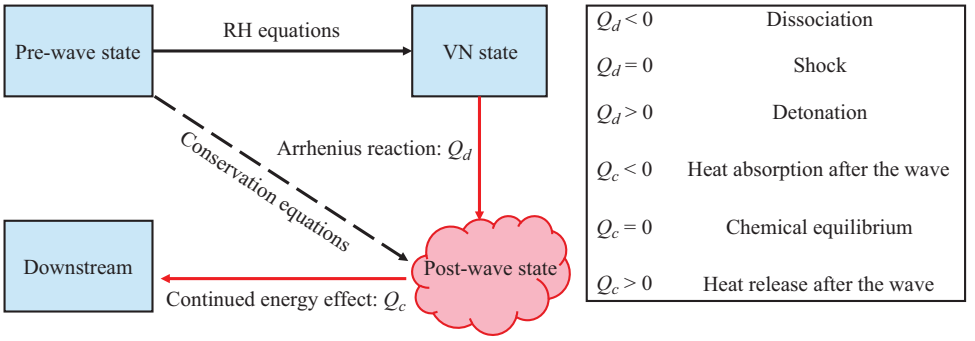

Figure 4. Analysis of the various energy effects on the curved shock including detonation and dissociation.

the effect of the chemical reaction to an energy release treatment, like the CJ theory did. Quantitatively speaking, the smaller errors of the two equations in the solution of post-wave parameters are demonstrated in table 1. Thus, the CDE will be the main one to be applied in the subsequent analysis and applications. Similar analysis and applications can also be performed for the CDEC, but these will not be repeated for the brevity of the article. It should be specifically noted that for some cases, CDEC is necessary such as when the effect of the chemical reaction zone on the curvature of the streamlines cannot be ignored in the two-dimensional problem.

With the help of CDE, the effect of energy release on the zero- and first-order parameters can be analysed separately, as shown in figure 4. For the zero-order parameters, according to classical gas dynamics knowledge, if energy release Q_d increases from zero, the p_2/p_1 will become smaller. It is known that the post-wave Mach number of a detonation wave is decreased compared with that of a shock wave, which means that the energy release decreases the post-wave Mach number. The detonation angle is also greater than the shock angle. For the first-order parameters, according to (2.5*a–d*), if $M_2^2 > 1$, then the energy release Q_c increases, and all three energy factors H, N and J will increase. Conversely, if $M_2^2 < 1$, then H and N will decrease. In short, the energy release has different effects on the zero- and first-order parameters in different situations, and the final effect will not always monotonically increase or decrease the post-wave gradient. This conclusion is also consistent with the patterns of variation in the influence coefficients. In general, the pre-wave pressure gradient has the greatest influence on the post-wave pressure gradient, and the energy release will significantly increase the effect of the pre-wave gradients on the post-wave pressure gradient. This provides a reference for the change in the pressure gradient in the post-wave of detonation.

3. Analysis with curved detonation equations in influence coefficient format

To better understand the curved detonation equations constructed in the previous section, further analysis will be performed in this section. We first solve the format of the influence coefficients of the post-wave gradients and discuss their variation. The detailed derivation can be found in Appendix D. The effects of energy release are highlighted; it not only affects the zero-order parameters such as M_2, but also changes the first-order gradients through the H, N and J coefficients. After this, post-wave gradients under different curvatures are fully discussed to emphasize the impact of curvature when compared with oblique detonation.

3.1. *Analysis with the influence coefficients of the pre-wave gradients*

As can be seen from Appendix D, the five influence coefficients can be divided into two parts: the former three represent the influence of pre-wave gradients (e.g. J_p, J_d, J_g) and the latter two (e.g. J_a, J_b) represent the influence of curvature. The influence coefficients of the pre-wave gradients are analysed first; after this, the influence coefficients of the two curvatures are discussed separately because the planar and transversal curvatures have different characteristics. It is worth noting that the specific curves of influence coefficients have a strong relationship with the incoming flow parameters. The detailed parameters given by the example are not universal for all detonation conditions, but the fundamental laws are similar. The incoming flow parameters given in this section are

$$p_1 = 1 \times 10^5\,\mathrm{Pa}, \quad \rho_1 = 0.1\,\mathrm{kg\,m^{-3}}, \quad M_1 = 10, \quad \gamma_1 = 1.3. \tag{3.1a–d}$$

To emphasize the influence of energy release in the detonation wave, various different situations of energy release are considered. When the energy release Q_d is negative, it means that the shock wave is energy absorbing, which can occur in the dissociation of air. When the energy release Q_d is positive, it means that the shock wave is exothermic, which can occur in a detonation wave. Similarly, when the energy release Q_c after the wave is negative, this means that there is an energy-absorbing chemical reaction after the wave, which can occur in a pathological detonation. When the energy release Q_c after the wave is positive, it means that there is an exothermic chemical reaction after the wave, which may mean that the detonation wave continues to combust after the wave.

The first concern is the effects of the pre-wave pressure gradient, streamline curvature and vorticity on the post-wave pressure gradient, as shown in figure 5. The solid line indicates a shock wave with no energy release and the area charts represent the effects of energy, where the lighter areas show energy absorption ($Q_d < 0$ or $Q_c < 0$) and the darker areas show energy release ($Q_d > 0$ or $Q_c > 0$). Thus, two aspects should be considered: one is how the influence coefficient varies with different wave angle and the other is how the influence coefficient is affected by various energy release. In figure 5(*a*), the solid blue curve shows that when the wave angle is between 20° and approximately 75°, the influence coefficient J_p always remains constant at approximately the same level, and it then decreases to 0. After exceeding approximately 84°, this effect becomes a negative correlation and gradually increases to a peak negative value over −1000. This curve will reach a maximum at 90°, meaning that a normal detonation wave has the largest influence coefficient when compared with oblique/curved detonation waves. In addition, at values of approximately 84°, the pressure gradient of the incoming flow has no effect on the pressure gradient behind the wave. The solid green curve, which represents the influence coefficient J_d, shows that the pre-wave streamline curvature makes a negative contribution to the post-wave pressure gradient for all wave angles. In the range of acute angles, this action law first increases gradually, then decreases to a minimum, and it reaches its maximum value at approximately 85°. Moreover, this contribution is 0 at the 90° point. This means that for positive detonation, the pre-wave streamline curvature has no effect on the post-wave pressure gradient at this point. The solid red curve, which represents the influence coefficient J_g, reveals that the contribution of the pre-wave vorticity to the post-wave pressure gradient is similar to that of the green curve, peaking at approximately 85°. In figure 5(*b*), the pattern of the effect of energy release (Q_c) is however different, for example, for the blue curve J_p, the peak of the effect is no longer located at 90°, whereas both J_d and J_g take their maximum at 90°. This difference occurs because the energy effects of the two types act in different ways.

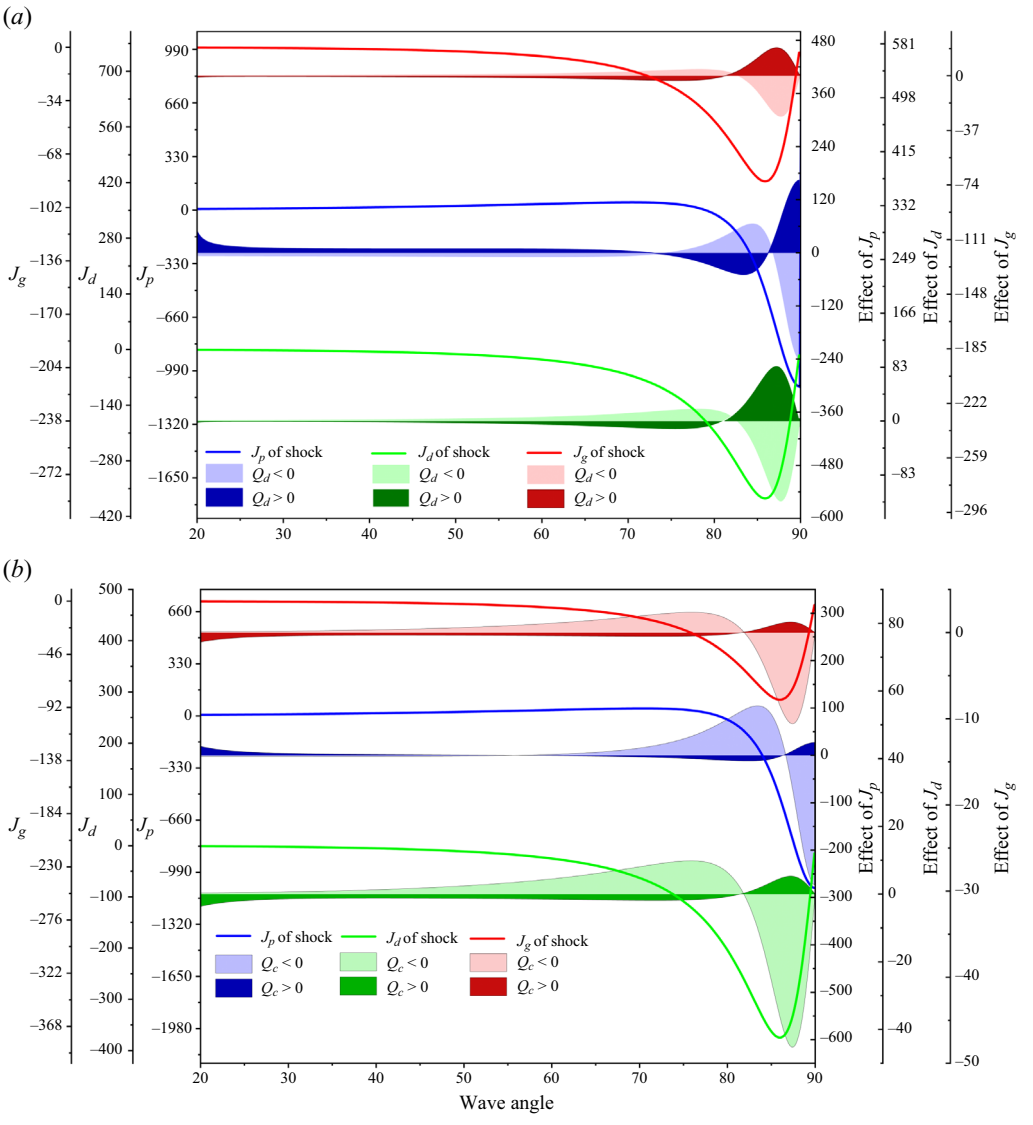

Figure 5. Influence coefficients of pre-wave gradients to the post-wave pressure gradient. (*a*) Q_d with positive, zero and negative values. (*b*) Q_c with positive, zero and negative values.

Figure 6(*a*,*b*) depicts the influence of pre-wave gradients on the post-wave streamline curvature. It can be seen from the solid blue curve that K_p keeps positive when wave angles are small, which means that the pre-wave pressure gradient will enhance the post-wave streamline curvature in this range. The curve subsequently becomes negative after crossing a point over 50°. As the wave angle continues to increase, the pre-wave pressure gradient has less effect and reaches a minimum. When it reaches 90°, there is no effect on the post-wave streamline curvature, which means that no matter how much the pressure is changed, the post-wave streamline curvature will not be affected. It can be seen that the solid green curve K_d rises from the acute angle range and reaches a maximum value near 90°. The solid red curve K_g shows that the influence law is similar to that of the green curve, but the values are smaller.

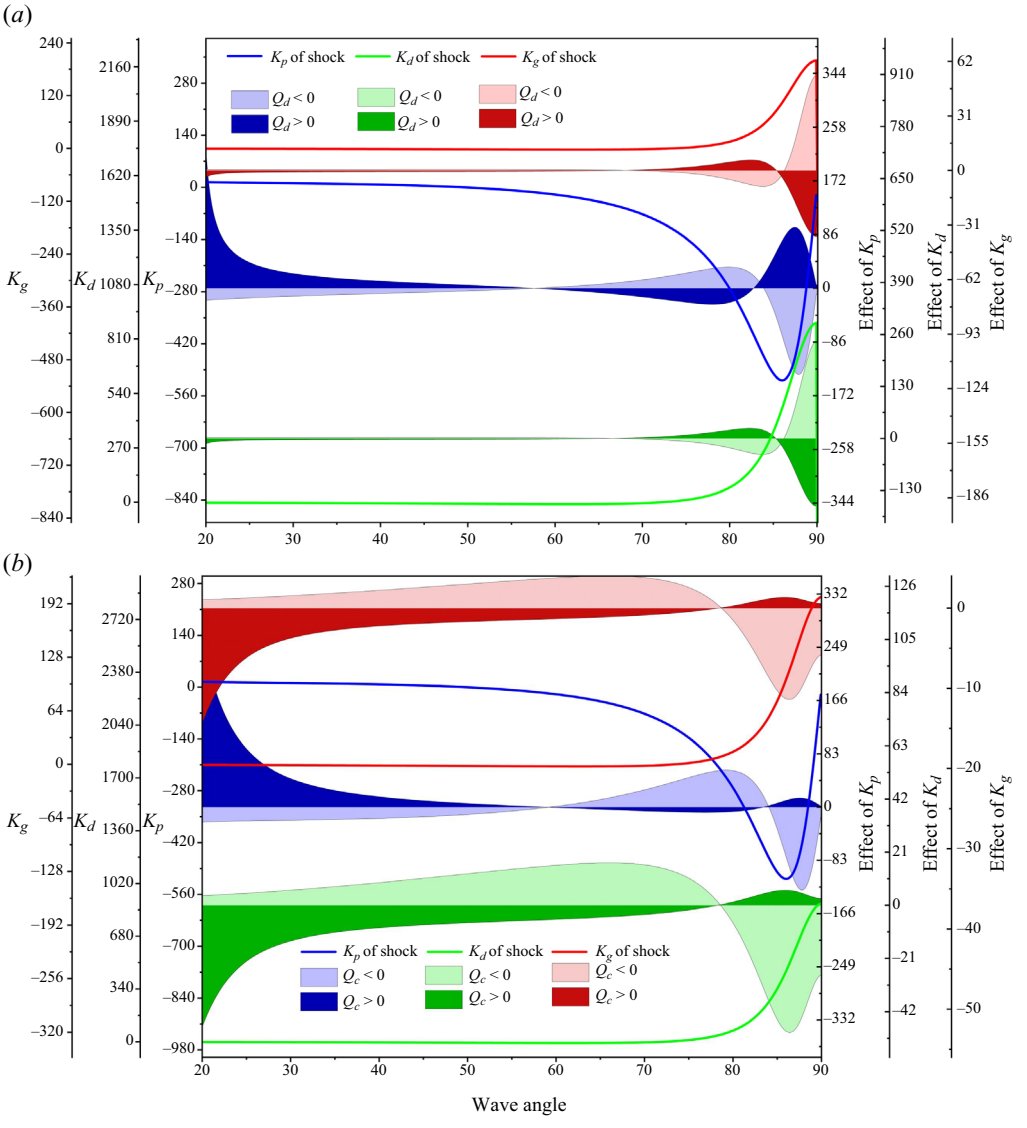

Figure 6. Influence coefficients of pre-wave gradients to the post-wave streamline curvature. (*a*) Q_d with positive, zero and negative values. (*b*) Q_c with positive, zero and negative values.

The effect of energy release in K_p is larger when the wave angle is smaller, which can be seen in the area chart in figure 6(*a*,*b*), and it gradually decreases as it approaches approximately 60°. This means that at smaller wave angles, the energy release causes a significant change in the effect of the pre-wave pressure gradient on the post-wave streamline curvature; conversely, in a normal detonation wave, the effect of the energy release in K_p is very small. In figure 6(*a*), the pattern of the green areas are different, and the green areas becomes 0 near 86°. This means that at this point, the pre-wave streamline curvature has an equal influence on the post-wave streamline curvature for the shock, dissociation and the detonation; after that, the effect of the detonation and dissociation wave is significantly stronger than that of the shock wave. The changes in the green and red line as well as areas are similar, and this implies that the pre-wave vorticity and streamline curvature make similar contributions to post-wave streamline curvature.

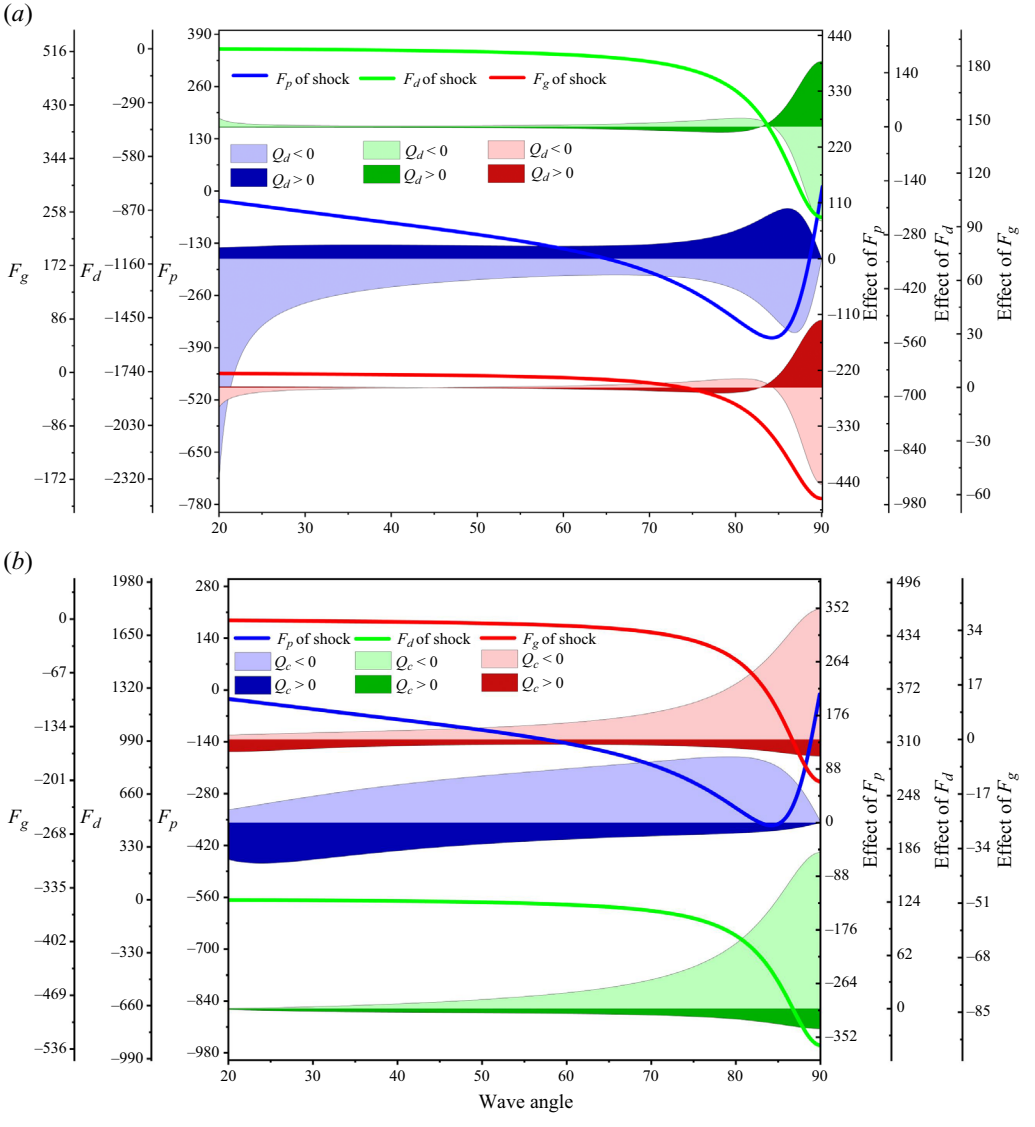

Figure 7. Influence coefficients of pre-wave gradients to the post-wave vorticity. (*a*) Q_d with positive, zero and negative values. (*b*) Q_c with positive, zero and negative values.

Generally speaking, the post-wave streamline curvature is most affected by the pre-wave streamline curvature and the maximum is achieved in a normal detonation wave; this is easy to understand intuitively and it is consistent with the laws of physics.

Figure 7 shows the variation of post-wave vorticity with incoming flow conditions. The blue curve F_p first decreases and then increases in the range of negative values, reaching a maximum just over 80°. The coefficient is zero at 90°, which means that the pre-wave pressure gradient does not affect the post-wave vorticity in normal detonation. The variation trends in the green curve F_d and the red curve F_g are similar, but their specific values are different. Both curves reach their maximum absolute value at 90°, and they are not zero-valued at any point, which means that these two coefficients are always present across the whole angular range. The blue areas are in opposite positions in figure 7(*a*,*b*), which means that the effects of Q_d and Q_c are different, with Q_d enhancing

the effect of F_p and Q_c weakening the effect of F_p. A similar analysis applies to the Q_d and Q_c for F_d and F_g. Figure 7 also shows that the pre-wave streamline curvature is still the biggest factor affecting the post-wave vorticity, and this is followed by the pre-wave pressure gradient and vorticity.

In these three figures, the pre-wave streamline curvature and vorticity action laws are always similar. This may be caused by the presence of the same parameter: $\partial\sigma/\partial s$. In addition, we can see that energy release always has a significant effect, which means that separate research is required to examine detonation waves, dissociations and simple shock waves. The fundamental reason for this difference is that the energy release will change the post-wave zero-order parameters with the influence coefficients of first-order gradients, and it will thus also change the first-order gradients. The energy release at different locations has completely different effects on the post-wave first-order gradients and these effects are also non-monotonic. These curves and their analysis help us to understand more clearly the variation patterns of detonation, and they also highlight the effect of energy release.

3.2. *Analysis with influence coefficients of detonation curvature*

Now that the pre-wave influence coefficients have been analysed, analysis with the influence coefficients of the detonation curvature should be performed. To exclude the influence of pre-wave gradients, the incoming flow parameters are set to be uniform, which means that the equations with influence coefficients can be simplified to

$$\left.\begin{aligned} P_2 &= J_a S_a + J_b S_b, \\ D_2 &= K_a S_a + K_b S_b, \\ \Gamma_2 &= F_a S_a + F_b S_b. \end{aligned}\right\} \tag{3.2}$$

The post-wave gradients will be different for planar and axial problems; as such, the system is examined separately from these two perspectives.

3.2.1. *Analysis with influence coefficients of planar curvature*

For two-dimensional curved detonation waves, there is no transversal curvature, which means that S_b is zero. Then, (3.2) can be simplified to

$$\left.\begin{aligned} P_2 &= J_a S_a, \\ D_2 &= K_a S_a, \\ \Gamma_2 &= F_a S_a. \end{aligned}\right\} \tag{3.3}$$

In such a case, the post-wave first-order gradient parameters are drawn as shown in figure 8. The curvature is set to -1, which means that $P_2 = -J_a$, $D_2 = -K_a$ and $\Gamma_2 = -F_a$.

In figure 8, the blue curve shows that under a given uniform incoming flow and constant curvature, the post-wave pressure gradient reaches its absolute maximum at 90°. This means that the post-wave pressure gradient will be at its maximum when oblique detonation is converted to normal detonation. In addition, at approximately 85°, the post-wave pressure gradient is zero; this is referred to as the Thomas point (Thomas 1947). The effect of energy release is always apparent, especially when the wave angle is small. The green curve represents the post-wave streamline curvature. This first increases and then decreases in the acute angle range, and it reaches a maximum at approximately 83°. In addition, the post-wave streamline curvature is zero at approximately 76°; this is an

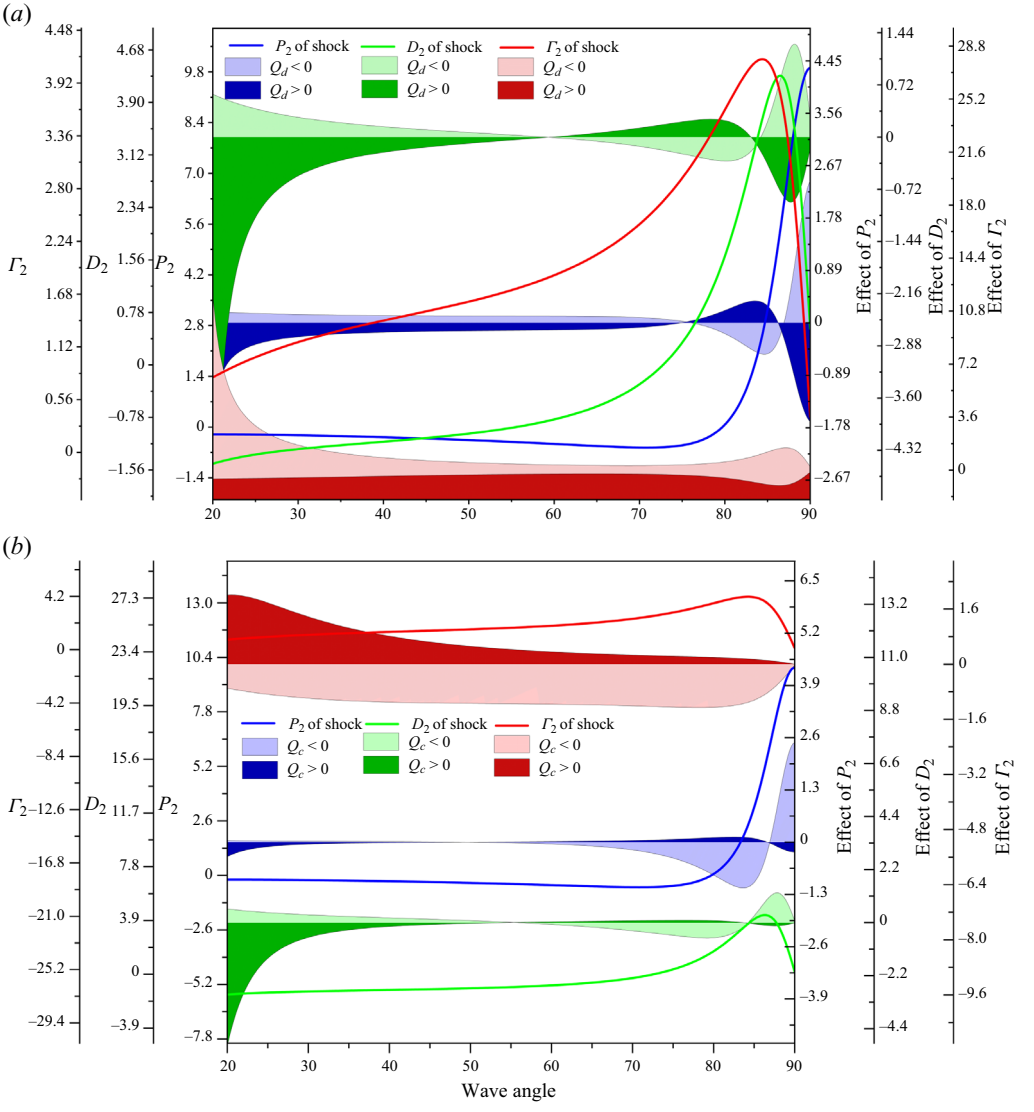

Figure 8. Post-wave first-order gradients of two-dimensional detonation waves in uniform flow. (*a*) Q_d with positive, zero and negative values. (*b*) Q_c with positive, zero and negative values.

important parameter to determine the flow situation after the wave, and it is called the Crocco point (Crocco 1937). The red curve represents the change of post-wave vorticity, which first increases and then decreases in the acute angle range, reaching a maximum at approximately 85°; the vorticity is zero at 90°. Another principle can be observed from figure 8: the energy release changes the locations of the Thomas and Crocco points, once again demonstrating that the effect of energy release is not negligible.

To illustrate the correspondence between these curves and the detonation wave more clearly, figure 9 displays the distribution of the streamline curvature after a curved detonation wave. Figure 9(*a*) shows several streamlines of the air dissociation flow field, where the chemical reaction takes the results of the study of Park (1985). Expressing the results of figure 9(*a*,*b*), it is not difficult to notice the effect of curvature on the flow. Herein, point 1 corresponds to the negative curvature of the streamline in figure 8, and

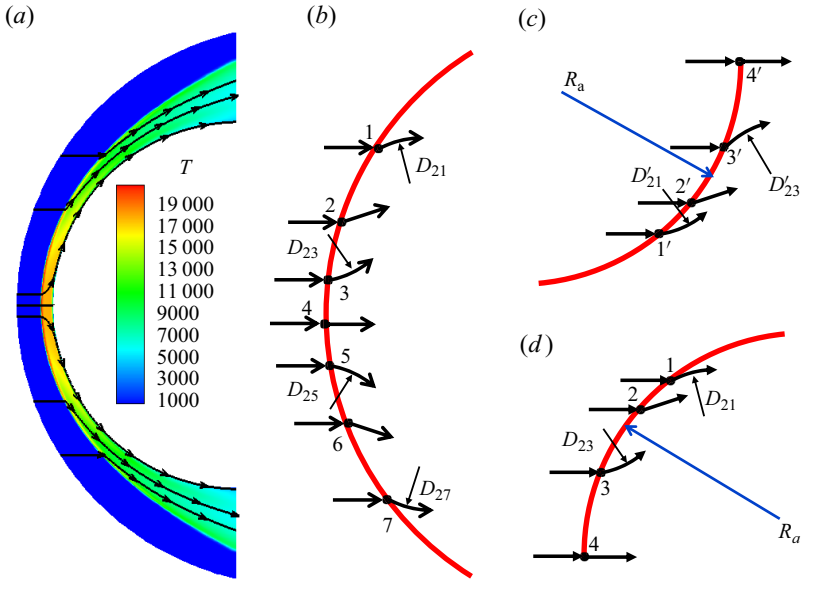

Figure 9. Post-wave streamline curvatures of a planar detonation wave in uniform flow. The initial conditions for the numerical simulation are pressure is 1.96 atm, temperature is 206 K, Mach number is 38 Mach and the incoming flow is pure air.

point 2 corresponds to the Crocco point, where the curvature of the streamline is zero. Point 3 is the positive curvature of the streamline after the Crocco point, and point 4 corresponds to the angle of the detonation wave being 90°, that is, a normal detonation wave. Points 5, 6 and 7 are then the positions in the obtuse-angle section corresponding to points 3, 2 and 1, respectively.

Curvature plays a crucial role in curved shocks and curved detonations. Therefore, it is necessary to investigate the effect of curvature on the post-wave gradients at different magnitudes and directions. The detonation curvatures can be varied in the planar and axial flow fields to observe the corresponding changes in the first-order gradients. With the above research purpose, we plotted the post-wave pressure gradient, streamline curvature and vorticity for five different detonation curvatures of -2, -1, 0, 1 and 2, as shown in figures 10, 11 and 12, respectively. In figure 10, different colours represent different magnitudes of detonation curvatures and concavity/convexity is distinguished by the solid/dashed lines. We can first conclude that changing the detonation curvature significantly affects the post-wave pressure gradient, and a larger detonation curvature will lead to an increase in the absolute value of the pressure gradient at all angles. This is consistent with our previous prediction. In addition, detonation waves with different curvatures have the same Thomas point, which means that the detonation curvature does not affect the Thomas point.

A similar regularity is also reflected in the post-wave streamline curvature, which is plotted in figure 11, in which it can be seen that a larger detonation curvature increases the curvature of the post-wave streamline across the full range of angles. Similarly, the position of the Crocco point remains unaffected by the detonation curvature. Figure 9(*c*) helps to illustrate the curvatures of the post-wave streamlines for different detonation curvatures more intuitively: figure 9(*c*) corresponds to the case with positive curvature, and its variation law has been explained in detail using figure 11; figure 9(*d*) corresponds to the case in which the detonation curvature is negative, and its variation law can also be seen in the obtuse part of figure 11.

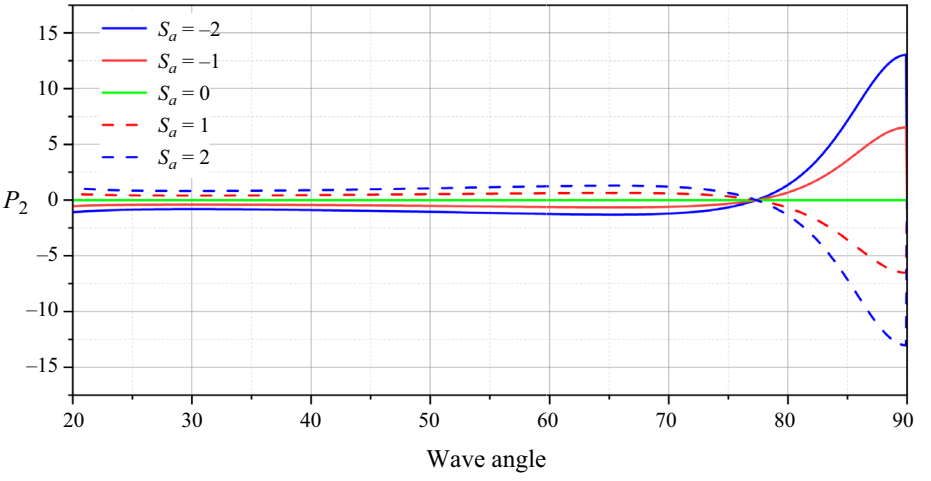

Figure 10. Post-wave pressure gradients with different planar curvatures S_a.

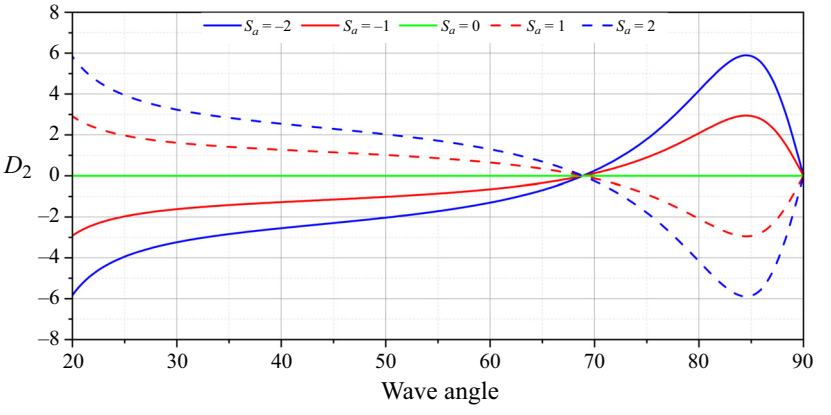

Figure 11. Post-wave streamline curvatures with different planar curvatures S_a.

Regarding the post-wave vorticity, we can conclude from figure 12 that this is always monotonous in the acute angle range, and increasing curvature also makes the vorticity larger. The same trend is followed in the obtuse angle range, but with the opposite sign. From the above three plots, it is not difficult to observe that the gradients of the concave and convex detonation waves are symmetric about the oblique detonation.

3.2.2. *Analysis with influence coefficients of axial curvature*

For an axial detonation wave, the curvature S_a is zero and the distance y is set to 1. The equations can thus be simplified to

$$\left.\begin{aligned} P_2 &= J_b S_b, \\ D_2 &= K_b S_b, \\ \Gamma_2 &= F_b S_b. \end{aligned}\right\} \tag{3.4}$$

In such a case, the post-wave first-order gradients are drawn as shown in figure 13. For the axial flow in figure 13, the blue curve shows that the post-wave pressure gradient is also

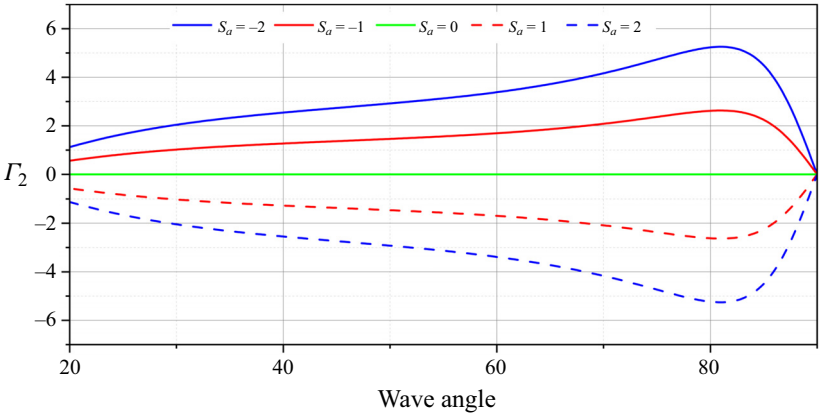

Figure 12. Post-wave vorticity with different planar curvatures S_a.

affected by the transversal curvature, which first decreases and then increases, reaching a maximum absolute value at approximately 86°. The green curve shows the effect of transversal curvature on the post-wave streamline curvature, reaching a negative maximum at approximately 82°. There is quite a significant difference when this is compared with planar flow: the energy release Q_d always enhances the post-wave pressure gradient and streamline curvature. The post-wave vorticity is not shown because the transversal curvature will not affect the post-wave vorticity, as also demonstrated by Mölder (2016).

Similar to the case of the planar detonation wave, we also plotted the curvature of the post-wave streamline in an axial flow with different detonation-wave angles, as shown in figure 14. Here, point 1 corresponds to the curvature of the streamline in the acute part of figure 13, and the direction of streamline curvature does not change in the process from point 1 to point 3; as with the planar case, the curvature in the normal detonation is zero. The changes in the obtuse angle range are similar and are not described in detail here. As with the planar curvature, to study the effect of different transversal curvatures on the post-wave gradients, we plotted five cases with curvatures of -2, -1, 0, 1 and 2, as shown in figures 15 and 16. In figure 15, in the acute angle range, the post-wave pressure gradients in the axial flow increase monotonically with increasing curvature. The biggest difference with the planar flow is the absence of Thomas points. Since the curvature value is given directly here instead of the distance y in the axial direction, this plot is not similar to the curve in figure 13.

When discussing the post-wave streamline curvature in the axial flow, we note that in figure 16, if the curvature is negative, the post-wave curvature of the streamline first increases and then decreases in the acute range, but it always remains positive; i.e. there is no Crocco point, which is completely different from the planar flow. This effect is similar when the curvature is positive. However, the curvature of the streamline increases across the range as the curvature of the detonation wave increases, which is similar to the planar flow. As discussed above, the transversal curvature does not affect the post-wave vorticity; as such, the post-wave vorticity is always zero for different curvatures, and this is not shown here specifically. From figure 16, we can see that the streamline curvature after an axial wave is monotonically related to the curvature of the detonation wave. When the transversal curvature is positive, the post-wave streamline curvature is negative, as shown in figure 14(*b*); accordingly, when the transversal curvature is negative, the post-wave streamline curvature is positive, as shown in figure 14(*a*).

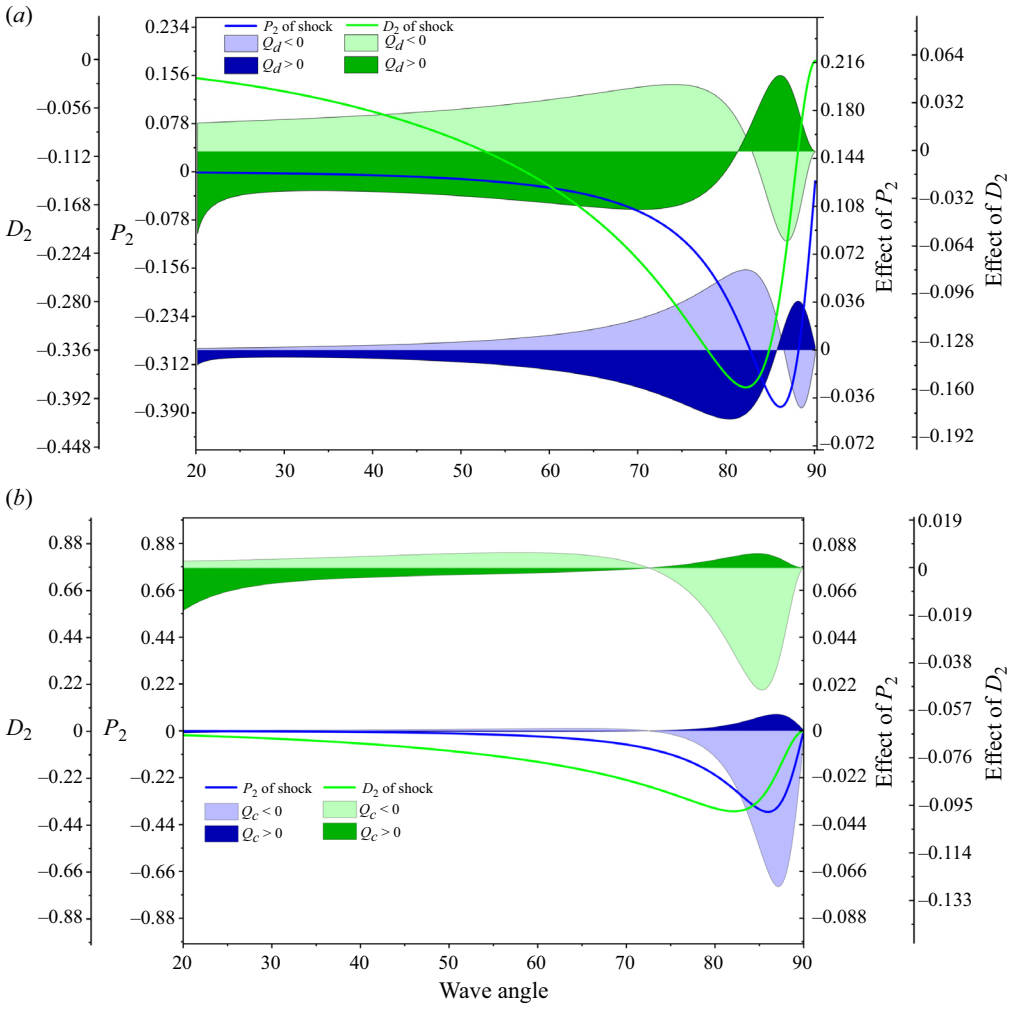

Figure 13. Post-wave first-order gradients of axial detonation waves in uniform flow. (*a*) Q_d with positive, zero and negative values. (*b*) Q_c with positive, zero and negative values.

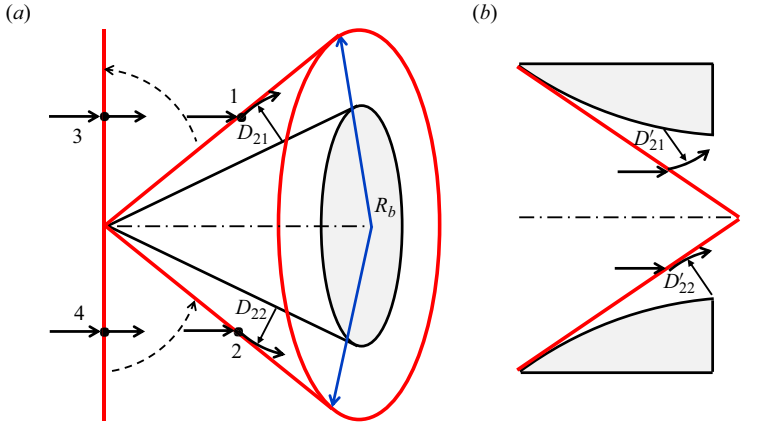

Figure 14. Post-wave streamline curvatures of an axial detonation wave in uniform flow.

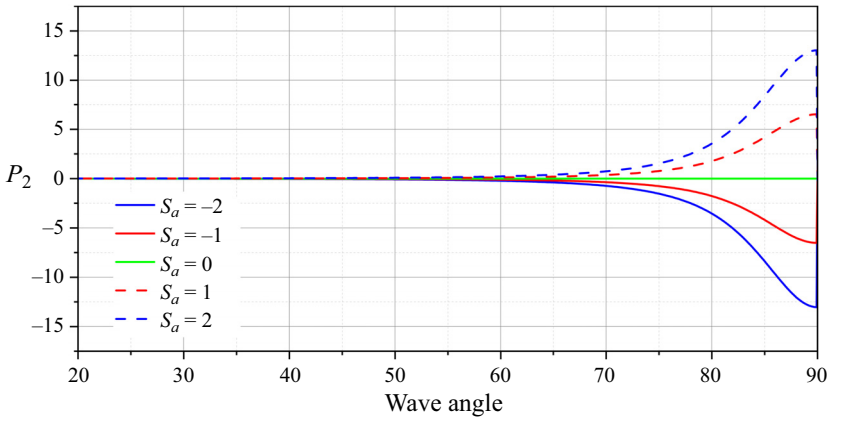

Figure 15. Post-wave pressure gradients with different transversal curvatures S_b.

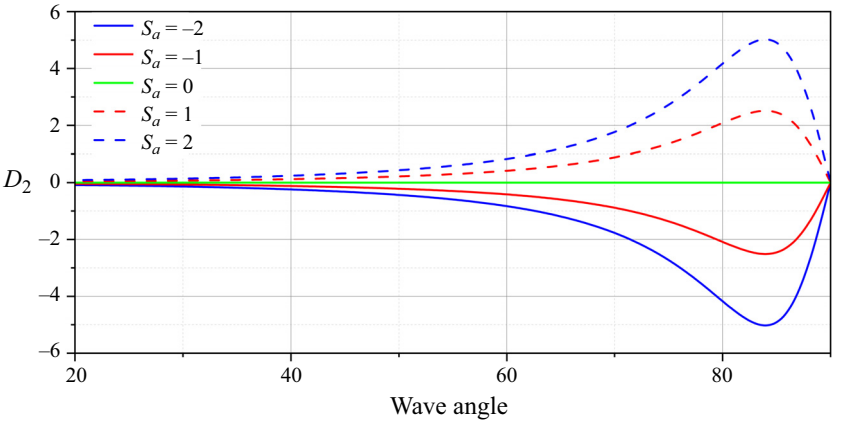

Figure 16. Post-wave streamline curvatures with different transversal curvatures S_b.

This section has considered the influence coefficients of curvature in curved detonation and the effects of different values of curvature on the post-wave gradients. These curves can be further applied in the analysis of curved detonation waves; for example, the presence of curvature leads to the divergence/convergence of the post-wave flow, which can change the post-wave temperature, density and pressure. This theory also provides a basis for subsequent analysis and application of detonation waves.

4. Verification of curved detonation equations

After the analysis of the curved-detonation equations, the next step is to verify the validity of the theory. It should be noted here that the theory makes several simplifications to the behaviour of a real detonation, and the value of the energy release is difficult to calculate completely correctly. Therefore, there will be differences between the theoretical and simulation results; the focus here is to study the common law reflected by the two results and explore the influence of energy release and curvature on curved detonation.

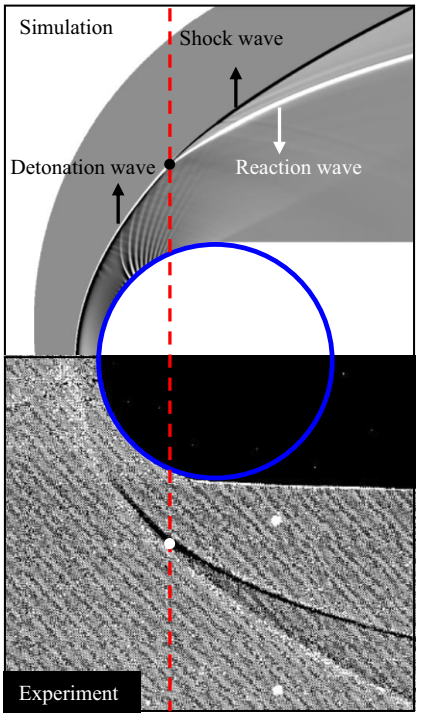

Figure 17. Comparison of the simulated and experimental results of a projectile-induced curved detonation: (*a*) shadowgraph of simulation result; (*b*) experiment by Lehr (1972).

4.1. *Comparison of post-wave pressure gradients between simulation and theory*

As noted before, the post-wave first-order gradient parameters can be derived from the curved-detonation equations for uniform incoming flow conditions. At the same time, we can also obtain the first-order gradient parameters by post-processing the results of the simulation. In this way, theory can be verified by comparing the results of two calculations. For this purpose, we have selected a projectile-induced curved-detonation result. The simulation approach provides a classical example, and this was verified in comparison with experiments, as shown in figure 17. Since the methods of numerical simulation are not the focus of this paper, they will not be described too much, and detailed explanations can be found in our previous study (Yan *et al.* 2024). Since aerodynamic parameters such as the post-wave pressure need to be used for comparison, the grid-independence of the numerical method needs to be examined and the detailed validation results can be found in Appendix E. Final results indicate that the grid level adopted in this paper can accurately capture data such as pressure and airflow deflection angle of the detonation. According to figure 17, it can be seen that the simulation results are in good agreement with the experimental results. Not only are the shapes of the detonation waves similar, but even the locations of the points where the shock and combustion waves separate are very close to each other. The reason for this separation is that as the intensity of the detonation wave decays, the induced shock wave is not strong enough to induce detonation combustion, so the induced shock wave and the combustion plane gradually separate, which is an inevitable phenomenon. Also this reminds us that only data prior to the separation point will be selected for subsequent verification. The incoming flow conditions were set to

$$p_1 = 42\,663\,\text{Pa}, \quad \rho_1 = 0.366\,\text{kg}\,\text{m}^{-3}, \quad M_1 = 6.39, \quad T_1 = 298\,\text{K}. \qquad (4.1a\text{–}d)$$

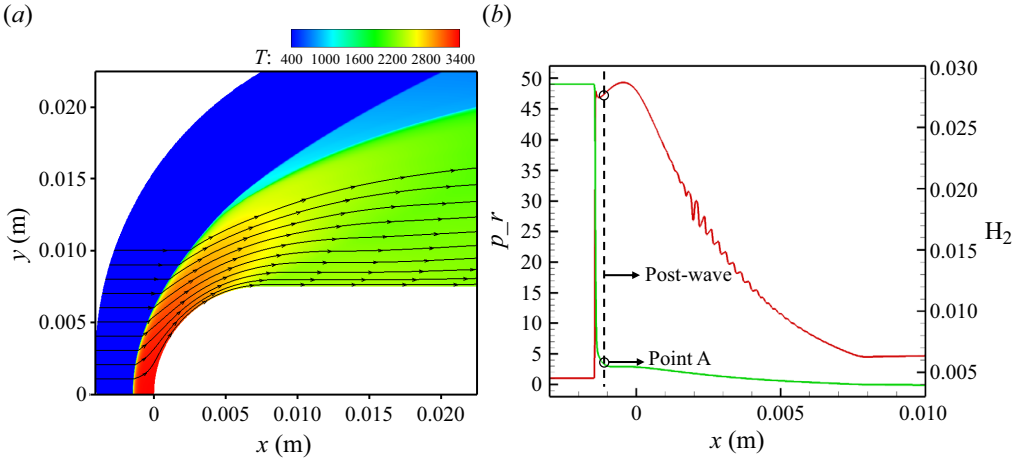

Figure 18. Simulation results: (*a*) temperature contour; (*b*) pressure and hydrogen mass fraction along the streamline.

The simulation results can be calculated consistent with the experimental incoming flow conditions as shown in figure 18(*a*). To quantify the gradient of the detonation wave, ten streamlines are selected in this paper and the variation of pressure and hydrogen content on any one of them is plotted, as shown in figure 18(*b*). It should be noted that these ten streamlines are all on the left side of the red dashed line in figure 17. In other words, the streamlines are located before the decoupling of the shock wave and reaction wave, so it can be considered as a detonation wave. Considering that the thickness of the detonation wave is not negligible, to extract the post-wave parameters, a uniform post-wave definition is adopted in this paper. Taking figure 18(*b*) as an example, the green curve indicates the mass fraction of hydrogen, which is 0.02851 in the incoming flow and becomes 0.00397 at infinity, which means that the total consumption of the gas is 0.0245. The point A after the wave is chosen, on which the mass fraction of hydrogen is 0.00592, and after calculation, it is known that the hydrogen consumed at this point accounts for more than 92 % of the total consumption; therefore, define this point as the post-wave.

Further, to more concretely show the change in pressure at the post-wave, four streamlines were selected, and the pressure and pressure gradient changes on them are plotted as shown in figures 19 and 20, respectively. From the four curves in figure 19, especially streamline 1, we can see that the first point at which the pressure value increases suddenly is the point referred to as the induced shock in the ZND model. After this, there will be a significant drop, which should correspond to the reaction zone in the ZND model. After this region, whether the pressure value rises or falls depends on the post-wave pressure gradient. In streamline 1, after the reaction zone of the detonation wave, the pressure value rises significantly, which means that the pressure gradient after the wave is positive; at the same time, we can notice that the pressure gradient behind the wave in streamline 1 in figure 20 is also greater than 0. In streamline 2, the pressure value rises less, meaning that the pressure gradient after the wave is less positive at this time; however, in streamline 3, the post-wave pressure value decreases slightly, implying that the pressure gradient is transformed to a negative value. Meanwhile, the pressure gradient behind the wave in streamline 3 becomes less than 0. Finally, in streamline 4, the pressure monotonically decreases. It can be seen that streamlines 2 and 3 are

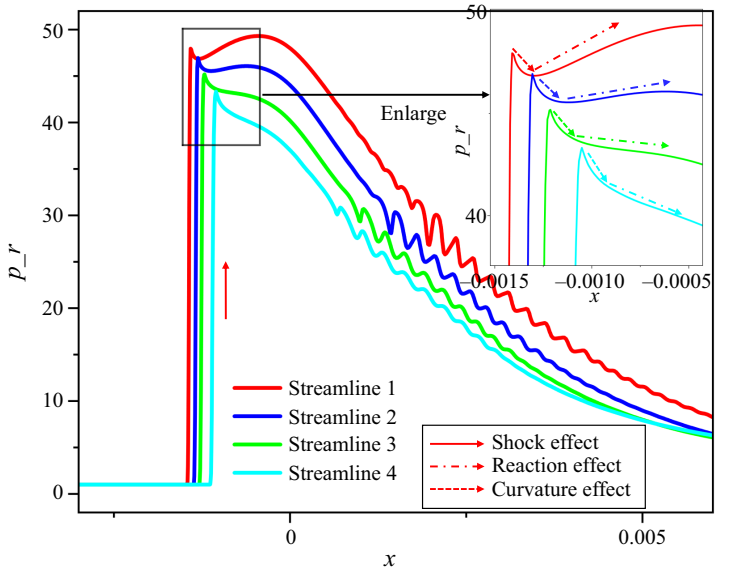

Figure 19. Pressure along the four streamlines extracted from simulation results.

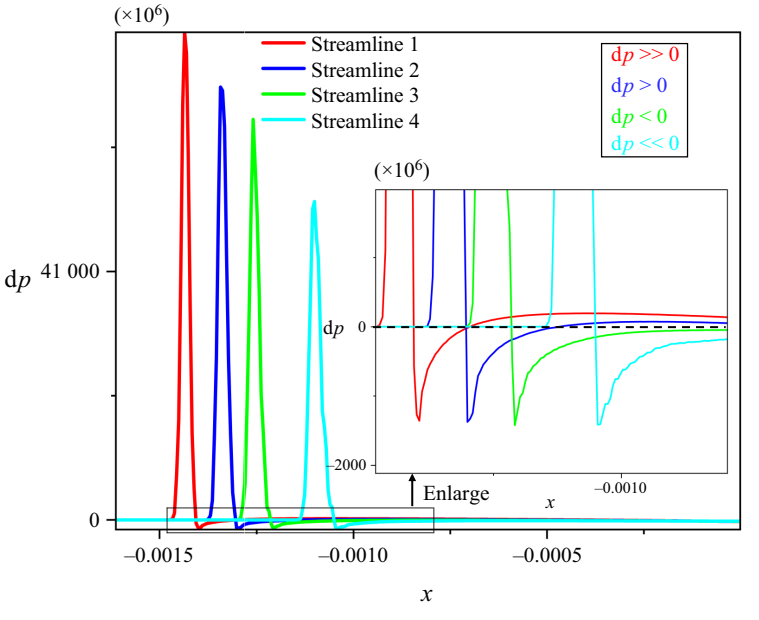

Figure 20. Pressure gradient along the four streamlines extracted from simulation results.

the two critical points at which the post-wave pressure gradient turns from positive to negative.

As noted earlier in the paper, if we want to calculate the post-wave pressure gradient using the curved-detonation equations, the incoming flow conditions and the curvature of the detonation wave should be known. The energy release is chosen to be 4.38 as Lehr (1972) described. The other incoming flow conditions remain the same as the simulation

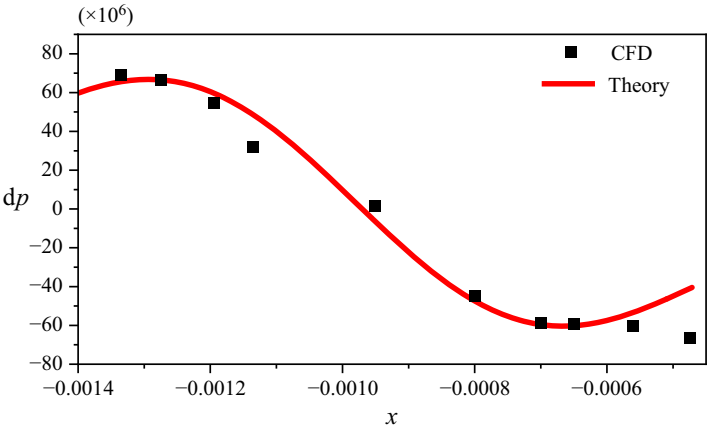

Figure 21. Comparison of the post-wave pressure gradient: the red curve is calculated from the curved detonation equations, the black squares are from the simulation results.

conditions, and the shape of the detonation wave can be obtained by the equation

$$y = 1 \times 10^{12}x^5 + 3 \times 10^9x^4 + 2 \times 10^6x^3 - 739.64x^2 + 1.5684x + 0.006. \tag{4.2}$$

From the curved detonation equations, the pressure gradient along the x direction can be expressed as

$$\frac{\partial p}{\partial x} = \frac{\partial p}{\partial s}\frac{\partial s}{\partial x} + \frac{\partial p}{\partial n}\frac{\partial n}{\partial x} = \rho V^2 P\cos\delta - \rho M^2[ND + (\gamma - 1)J]\sin\delta. \tag{4.3}$$

With the above calculation parameters, the curved detonation equations can be used to calculate the post-wave pressure gradient along the x direction, as shown in figure 21.

In figure 21, the red curve is the theoretical post-wave pressure gradient calculated from the curved detonation equations and the black squares are the post-wave pressure gradient data extracted from the simulation results for ten streamlines. It is obvious that the theoretical post-wave pressure gradient is in good agreement with the simulation results and the overall pattern of variation is similar, which indicates that the theory proposed in this paper is valid and applicable. The errors may be due to the following aspects: errors in the fitting of the detonation wave, errors in the energy release, errors in the extraction of data, etc. Furthermore, the theory does not require the complex calculations needed by simulations when obtaining the post-wave gradient, so it can be used as a rapid means of prediction.

4.2. *Comparison of post-wave streamline curvature between simulation and theory*

The previous section introduced a comparison of the pressure gradient. Further to this, in this section, a comparison of the streamline curvature is performed. In a similar way, we also selected four streamlines in the detonation flow field, named streamlines 5–8. Then, the airflow-deflection angles and streamline curvatures of the four streamlines were plotted in turn against their x-axis coordinate, as shown in figure 22 and 23.

In figure 22, common trends can be discovered about the airflow-deflection angles: the pre-wave airflow-deflection angles are zero and they rise rapidly after the induced shock; then, in the ZND structure of the detonation wave, after the induced shock, the airflow-deflection angles all experience a significant drop. However, the four streamlines

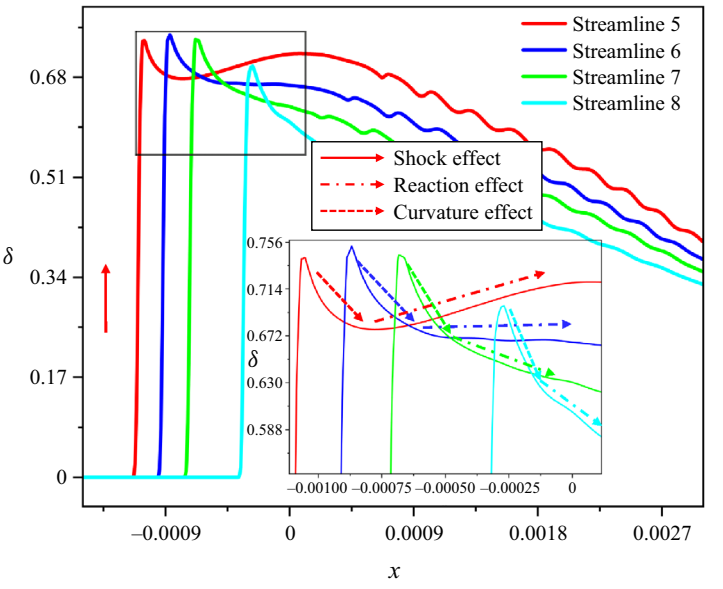

Figure 22. Deflection angle along the four streamlines extracted from simulation results.

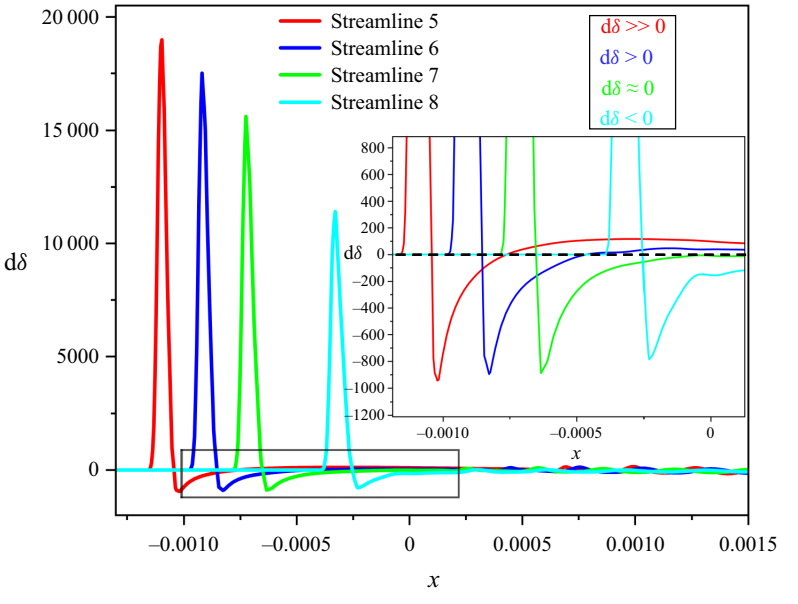

Figure 23. Streamline curvature along the four streamlines extracted from simulation results.

differ in the trend of the post-wave airflow-deflection angle. In streamline 5, the post-wave airflow-deflection angle obviously rises; this means that the post-wave streamline curvature is positive at this time. With the right shift of the x coordinate, in streamline 6, the level of this rise has decreased, which means that the curvature is still positive, but its value has been reduced. Then, in streamline 7, the post-wave airflow-deflection angle changes from increasing to decreasing; this implies that the streamline curvature at this point changes from positive to negative. Finally, in streamline 8, the magnitude of the

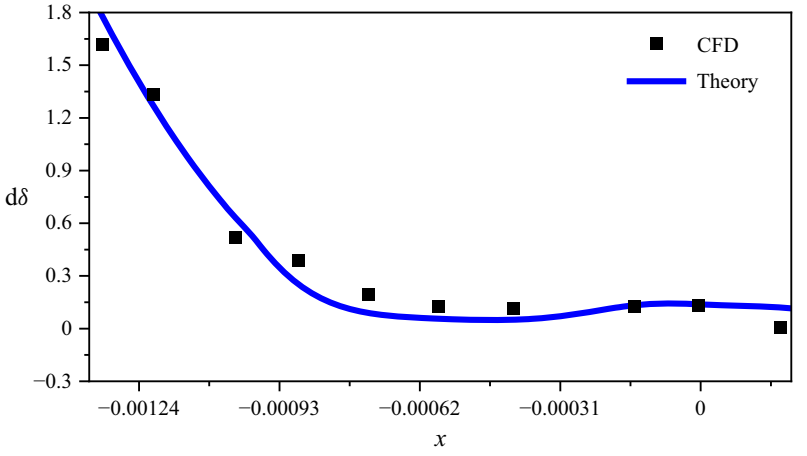

Figure 24. Comparison of the post-wave streamline curvature: the blue curve is calculated from the curved detonation equations, the black squares are from the simulation results.

decrease further increases. These changes also correspond to the streamline curvatures in figure 23. The gradients of streamlines 5 and 6 are greater than 0, and the gradients of streamlines 7 and 8 are less than 0.

From the curved detonation equations, the curvature of the streamlines along the x direction can be expressed as

$$\frac{\partial \delta}{\partial x} = \frac{\partial \delta}{\partial s}\frac{\partial s}{\partial x} + \frac{\partial \delta}{\partial n}\frac{\partial n}{\partial x} = D\cos\delta + (HM^2 - 1)P\sin\delta. \tag{4.4}$$

To compare the equation results with the simulation results, we calculated the corresponding post-wave streamline curvature under the same conditions as shown in figure 24. Similarly, in figure 24, the blue curve is the streamline curvature after the wave calculated according to the curved detonation equations, and the black squares are the streamline curvature in the simulation results. It can be seen from the figure 24 that the curve is in good agreement with the point, and the overall law is similar. It is further proved that the curvature of the streamline after the wave calculated by the curved detonation equations is correct and reasonable.

The above comparative analysis of the pressure gradient and streamline curvature shows that the theoretical calculation method proposed in this paper is effective and has good prospects for practical application to detonation. If a researcher seeks to determine the post-wave pressure gradient and streamline curvature based on the incoming flow conditions and the shape of the detonation wave to analyse the flow field of the detonation, the theoretical method presented here can be used without the need for simulations, which was the purpose of this study.

5. Application of curved detonation equations to polar analysis

Polar analysis of detonation is a common and effective method that is used in theoretical research examining oblique detonation waves and other detonation phenomena (Pratt, Humphrey & Glenn 1991). Through Appendix A, we can obtain the relationship between the wedge angle and the detonation wave angle, and by plotting this relationship, we can get the polar curve. Previous polar analysis has often been based on the zero-order parameters. However, the curved detonation equations proposed in this paper can obtain

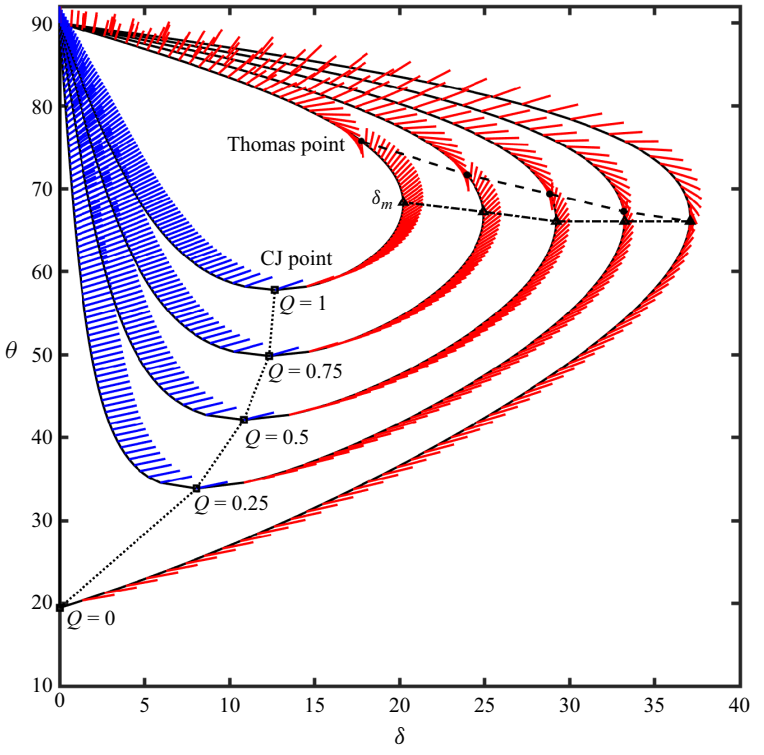

Figure 25. Polar analysis of detonation waves with post-wave gradients/streamline curvatures in planar flow. The x-coordinate represents the wedge angle δ and the y-coordinate is the detonation wave angle θ.

the relationships for the first-order gradients of a detonation wave. Therefore, analysis of the first-order gradients can be added to the previous polar curve, and thus, the variation law and relationship between the first-order gradients can be studied. This gives us a new method for analysis of the polar curves of detonation waves.

5.1. *Pressure gradient/streamline curvature polar for two-dimensional curved detonation waves*

Figure 25 shows polar analysis plots of two-dimensional curved detonation waves for different energy releases. For this analysis, the Mach number was set to 10, the value of planar curvature S_a was -1, and the transverse curvature S_b was zero. Similarly, to simplify the problem, the incoming flow was set to be uniform, and $P_1 = D_1 = \Gamma_1 = 0$. In oblique detonation, the relationship between the wedge angle and the detonation wave-angle is given by Pratt *et al.* (1991). Here, we define a slope l to represent the changing relationship between the post-wave pressure gradient and the streamline curvature:

$$l = \frac{P_2}{D_2} = \frac{\dfrac{1}{\rho V^2}\dfrac{\partial p}{\partial s}}{\dfrac{\partial \sigma}{\partial s}} = \frac{1}{\rho V^2}\frac{\partial p}{\partial \sigma}. \tag{5.1}$$

This slope has a wide range of applications in shock waves and it can be used to study shock-wave phenomena such as Mach reflections. Interestingly, the same problem of

reflection also exists in detonation waves, so the study has very clear physical significance and application prospects.

The black lines in figure 25 show the relationship between the wedge angle (x-coordinate) and the detonation wave angle (y-coordinate), and the red and blue lines represent the slope l at their respective points: red represents over driven (OD) detonation and blue represents the solution of under driven (UD) detonation. The point at which OD meets UD is called the CJ solution, the maximum wedge angle at a defined detonation-wave angle is δ_m, and the range between the two is called the standing range of the detonation wave. Since the energy release will significantly affect the range of the polar curve, and to better compare with the shock wave, we calculated multiple detonation-wave polar curves under energy release values from 0 to 1. It is not difficult to see that when the energy release is 0, this polar curve represents a shock wave. It is worth noting that near the Thomas point, the slope l changes sign, and with increasing energy release, the detonation angle of the Thomas point increases, and the corresponding wedge angle decreases. In addition, in the shock wave, the Thomas point has the largest wedge angle, but the two do not coincide in a detonation wave.

Without the curved detonation equations, detonation polar curve analyses can only describe the variation law of the zero-order parameters. With the curved detonation equations, we can obtain more useful information about the first-order gradient, which is necessary for understanding the detonation phenomenon and exploring its evolution patterns. The analysis of the polar curves given in this paper is just an example; more first-order parameters, such as the gradients of density and velocity in the detonation wave, can be obtained by similar methods.

5.2. *Pressure gradient/streamline curvature polar analysis for axial detonation waves*

A polar curve analysis diagram was plotted for axial flow in the same way as that shown in figure 25; the planar curvature was changed to transversal curvature, but the other aerodynamic parameters were the same. The result is shown in figure 26. From figure 26, we can summarize the law as follows. Unlike the planar flow problem, in the axial flow, l remains constantly positive; this means that there is no Thomas point. In both the OD and UD detonation cases, l increases monotonically with increasing detonation-wave angle. This means that in axial detonation, the pressure will increase with increasing airflow-deflection angle. Together, this plot and its analysis illustrate that, with the help of the curved detonation equations, we can obtain the first-order gradient information of a detonation wave using polar curves. This also again clarifies the effect of energy release on the first-order gradients after the detonation wave. This not only greatly expands our means of analysing detonation, but it also deepens our understanding of the detonation phenomenon.

6. Application of curved detonation equations to detonation wave capture and inverse design

As mentioned before, the curved detonation equations give the relationship between the incoming flow, curvatures and post-wave gradients, we can solve the post-wave gradients from the incoming flow and curvatures. However, we can also solve the curvatures of detonation wave according to the known incoming flow and post-wave gradients. To capture the detonation wave, a third-order polynomial function is used to fit the shape of the detonation wave, and the shape of the detonation wave is determined by solving the coefficient term of the unknown polynomial function.

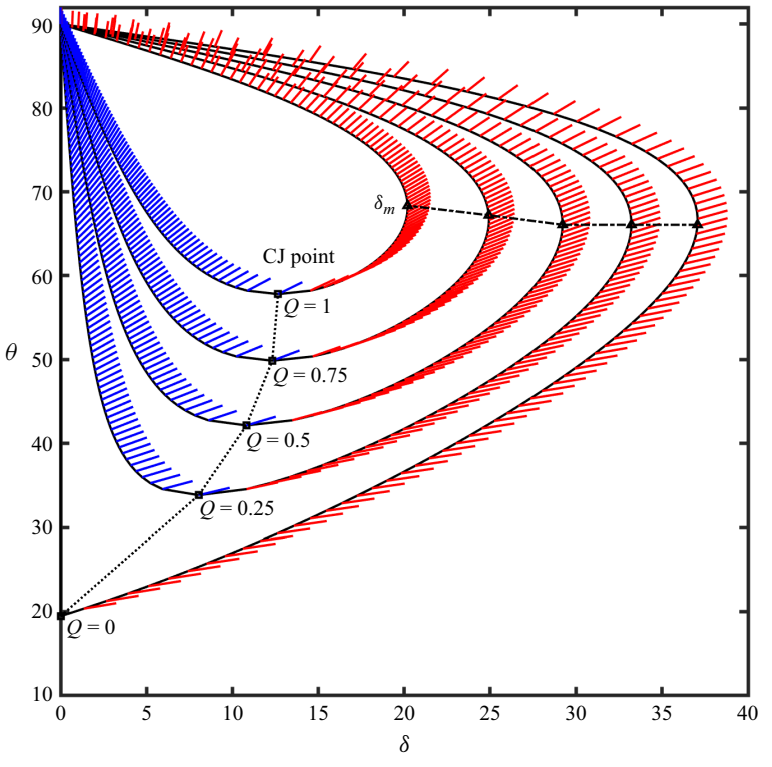

Figure 26. Polar analysis of detonation waves with post-wave gradients/streamline curvatures in axial flow. The x-coordinate represents the wedge angle δ and the y-coordinate is the detonation wave angle θ.

We draw the following flow chart in figure 27 to explain the overall process. First, a detonation wave with definite shape is given as y_0. This function is defined purely mathematically and has no reference to experiments or numerical simulations. Then, the curvatures of the detonation wave are solved according to its incoming flow conditions and post-wave parameters/gradients. After that, the second-order derivative of the detonation wave shape function is solved according to the curvatures, and then the polynomial interpolation function y are established. In this way, we get a polynomial fitted detonation wave shape function $y = ax^3 + bx^2 + cx + d$. Relationship between detonation wave parameters and its shape function:

$$y' = \tan\delta, \tag{6.1}$$

$$S_a = \frac{y''}{(1 + y'^2)^{3/2}}. \tag{6.2}$$

If the curved detonation equations were used, we can further solve the second derivative of the curve according to the curvatures, so we can establish a more accurate system of equations:

$$\left.\begin{aligned} ax_1^3 + bx_1^2 + cx_1 + d &= y_1 \\ ax_2^3 + bx_2^2 + cx_2 + d &= y_2 \\ 6ax_1 + 2b &= y_1'' \\ 6ax_2 + 2b &= y_2'' \end{aligned}\right\}. \tag{6.3}$$

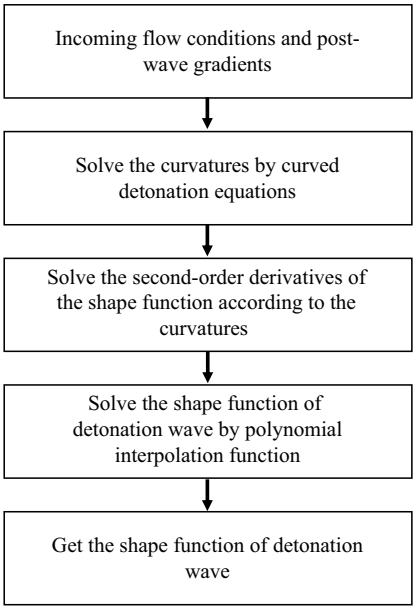

Figure 27. Flow chart of detonation wave capture based on curved detonation equations.

Moreover, it is clear that a shape function can be fitted based on the slope even without the curved detonation equations, as shown in the following equation. Therefore, to compare with the results, we likewise calculated the shape function based on the RH relations:

$$\left.\begin{aligned} ax_1^3 + bx_1^2 + cx_1 + d &= y_1 \\ ax_2^3 + bx_2^2 + cx_2 + d &= y_2 \\ 3ax_1^2 + 2bx_1 + c &= y_1' \\ 3ax_2^2 + 2bx_2 + c &= y_2' \end{aligned}\right\}. \tag{6.4}$$

6.1. *Capture for two-dimensional curved detonation wave*

To verify the feasibility of the above-mentioned detonation wave capture method, an example is given here. The given shock wave shape function is in (6.5), the shape function fitted with RH relations is (6.6), the shape function fitted with curved detonation equations is (6.7), as shown in figure 28.

$$y_0 = (e^x - 1)/2, \tag{6.5}$$

$$y_r = -0.3182x^3 + 0.7137x^2 + 0.4636x, \tag{6.6}$$

$$y_c = 0.0983x^3 + 0.3727x^2 + 0.3882x. \tag{6.7}$$

In figure 28, the blue curve is the originally given detonation wave shape function, the green curve is the detonation wave curve captured according to the RH relations and the red curve is the detonation wave captured according to the curved detonation equations. Obviously, the red curve is closer to the blue curve, which means that the method proposed in this paper can better fit the shape of detonation wave. This is attributed

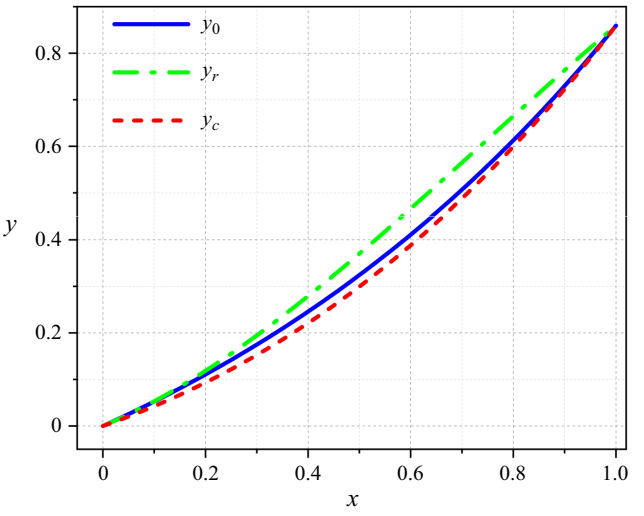

Figure 28. Comparison of the two methods to capture the two-dimensional curved detonation wave: y_0 is the given wave, y_r is the wave captured based on the RH relations and y_c is the wave captured based on the curved detonation equations. The incoming Mach number is 6 and the specific heat ratio is 1.3.

	Maximum error	*RSS*	R^2
RH	0.0583	0.1399	0.9776
CDE	0.0251	0.0322	0.9948

Table 2. Comparison between the RH relations and the curved detonation equations in planar wave capture.

to the higher-order accuracy of the curved detonation equations compared with the RH relations. For more accurate comparison, we also calculate the maximum error, sum of squares of residuals (*RSS*) and goodness of fit (R^2) of the two methods in table 2. In terms of maximum error, the maximum error obtained by curved detonation equations is 0.00251, while that obtained by RH relations is 0.00583, so the maximum error is reduced by 56.95 %. As for the *RSS*, which is 0.1399 according to the RH relations and 0.0322 according to the curved detonation equations, the *RSS* is reduced by 76.98 %. Finally, the R^2 value increases from 0.9776 to 0.9948, which means that the accuracy of fitting is increased also. These above data mean that the capture method based on curved detonation equations is effective.

6.2. *Capture for axisymmetric curved detonation wave*

Further, to verify the effectiveness of this method in the case of axisymmetric curved detonation, the wave with a given function and an axisymmetric curvature are selected in (6.8). The shape function of the detonation wave is calculated and the result of the

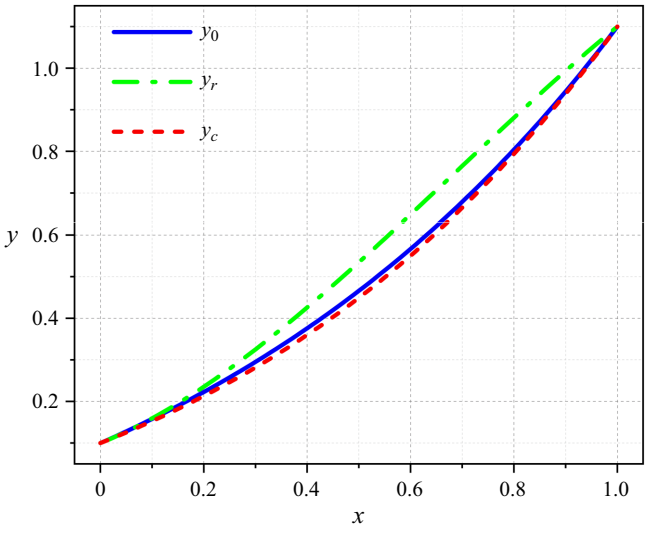

Figure 29. Comparison of the two methods to capture the axisymmetric curved detonation wave: y_0 is the given wave, y_r is the wave captured based on the RH relations and y_c is the wave captured based on the curved detonation equations. The incoming Mach number is 6 and the specific heat ratio is 1.3.

	Maximum error	*RSS*	R^2
RH	0.0862	0.3075	0.9635
CDE	0.0169	0.0144	0.9983

Table 3. Comparison between the RH relations and the curved detonation equations in axisymmetric wave capture.

calculation is given in (6.9) and (6.10). The capture results are shown in figure 29.

$$y_0 = (3^x - 1)/2 + 0.1, \tag{6.8}$$

$$y_r = -0.4723x^3 + 0.9700x^2 + 0.5023x + 0.1, \tag{6.9}$$

$$y_c = 0.2012x^3 + 0.3017x^2 + 0.4971x + 0.1. \tag{6.10}$$

It is not difficult to see from figure 29 that the red curve is obviously closer to the blue curve than the green curve. This means that the detonation wave capture method proposed in this paper is also applicable in the case of axisymmetric waves, which further proves the correctness of the method. Similarly, we calculated the error analysis for the two fitting methods as indicated in table 3. The maximum error obtained by curved detonation equations is 0.0169, while that obtained by RH relations is 0.0862, so the maximum error is reduced by 80.39 %. Then, as for the *RSS*, which is 0.3075 according to the RH relations and 0.0144 according to the curved detonation equations, the *RSS* is reduced by 95.32 %. Finally, the R^2 value increases from 0.9635 to 0.9983, which means that the accuracy is increased by 3.48 %.

The above two examples show that the detonation wave capture method proposed in this paper is suitable for two-dimensional and axisymmetric detonation. Compared with the

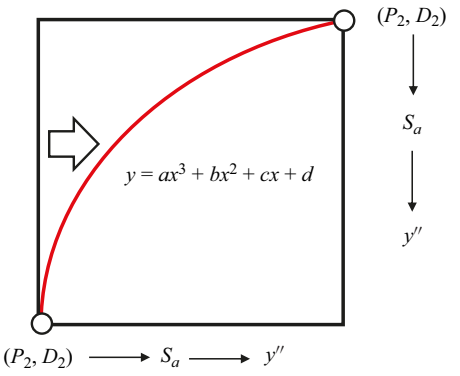

Figure 30. Schematic diagram of curvature solved from gradient.

	Case 1	Case 2	Case 3	Case 4	Case 5	Case 6	Case 7
P_2,D_2	(−0.3, −0.3)	(−0.2, −0.2)	(−0.1, −0.1)	(0, 0)	(0.1, 0.1)	(0.2, 0.2)	(0.3, 0.3)
S_a	(−1.386, −0.265)	(−0.924, −0.176)	(−0.462, −0.088)	(0, 0)	(0.462, 0.088)	(0.924, 0.176)	(1.386, 0.265)
y''	(−1.938, −1.274)	(−1.292, −0.849)	(−0.646, −0.424)	(0, 0)	(0.646, 0.424)	(1.292, 0.849)	(1.938, 1.274)

Table 4. Curvatures and second-order derivatives solved from the post-wave gradients.

fitting method with only zero-order parameters, the wave obtained by curved detonation equations has made great progress in all aspects.

6.3. *Inverse design based on curved detonation equations*

As described in previous subsections, the curvature of the detonation wave can be solved based on the first-order gradient of the pre-wave and post-wave. According to such an idea, if the post-wave pressure gradients and streamline curvatures are given, the curvature of the detonation wave can be solved. Thus, the shape of the detonation wave can be obtained to match the gradient requirements. The schematic diagram is given in figure 30.

In figure 30, the key parameters are the coordinates of the two design points and the first-order gradients. After which, the shape function of the detonation wave can be solved according to the curved detonation equations. In this paper, we give the following design parameters: $(x_1, y_1) = (0, 0)$; $(x_2, y_2) = (1, 1)$; $(P_2, D_2) = (-0.3, -0.3) - (0.3, 0.3)$. Under the above conditions, we can calculate the detonation wave curvature and the second-order derivatives of shape functions at different post-wave gradients as shown in table 4 and the shape of the detonation wave is shown in figure 31.

Table 4 shows the calculation results in seven different cases, and the detonation curve in figure 31 can be obtained according to results. From figure 31, a greater post-wave first-order gradient corresponds to a more obvious curvature, where the gradient of 0 results in an oblique detonation wave, while two gradients with opposite numbers are symmetrical about the oblique detonation wave. After obtaining the above detonation wave shape, we can further solve the shape of the wall according to the method of characteristics, thus the whole process of inverse design is completed. This part of the research can be further developed in future studies. Though this example is simple, the method is suitable to any given specific requirements. Therefore, the method proposed in this paper can be

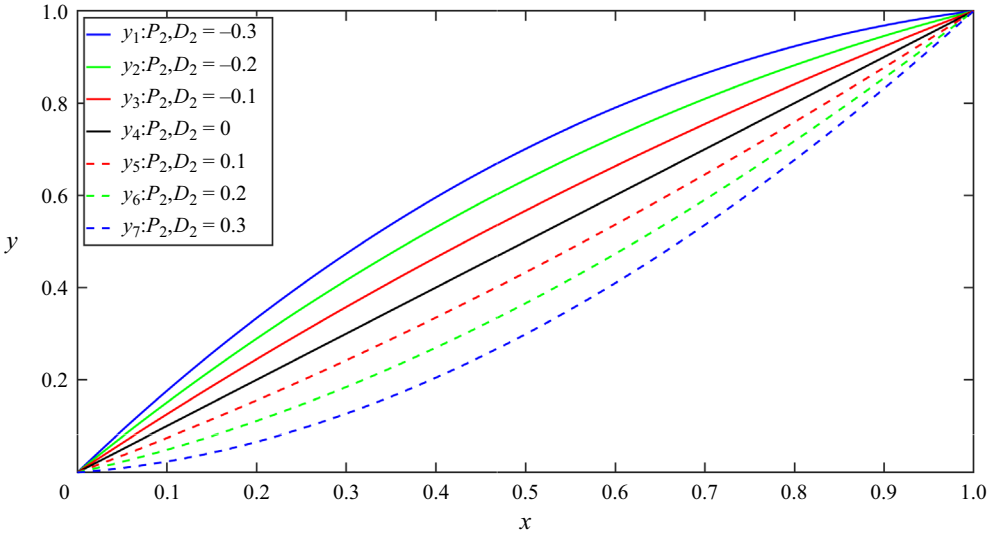

Figure 31. Detonation wave under different post-wave gradients.

considered as an effective means of inverse design of the detonation wave shape based on the post-wave gradient parameters.

7. Conclusions and prospects

To get the gradients in shock-induced chemical reactions, the curved detonation equations are established in this paper. Based on the curved shock theory and supplemented with the energy effect, the curved detonation equation is derived in the planar and axisymmetric flow. Both the mathematical derivation and the physical assumptions suggest that the equation is applicable to universal problems of shock-induced chemical reactions such as detonation and dissociation. The subsequent analysis of the influence coefficients reveals the variation of the post-wave gradients with an emphasis on the influence of energy release and curvatures by comparison with the shock and oblique detonation. These analyses contribute to a better understanding of the detonation, such as the curvature of the streamline and the variation of pressure. The theoretical values calculated by the curved detonation equations were proved to be accurate and reliable by comparing with the post-wave gradient parameters calculated from simulation. This verifies the correctness of the curved detonation equations. After verification, several applications were presented to illustrate the benefits and potential value. Polar analysis with gradients obtained from the curved detonation equations was proposed to provide a higher order perspective. These gradients will assist in the analysis of detonation reflections and provide valuable guidance. A wave capture method for detonation can also be created based on curved detonation equations. The accuracy of capture is significantly improved compared with the method with only zero-order parameters in both planar and axisymmetric examples. Furthermore, the combination of curved detonation equations with the method of curved-shock characteristics makes the inverse design of the detonation wave possible.

In the future, second-order curved detonation equations could be developed based on curved detonation equations to achieve higher-order parameters. In addition, detailed chemical reactions can be introduced into the curved detonation equations to provide a more accurate description of detonation waves. The potential applications of curved

detonation equations can be explored in the reflection and inverse design of detonation. Further applications of the curved detonation equations can be developed with respect to the study of the other shock-induced combustion phenomenon.

Funding. The authors acknowledge the support of the National Natural Science Foundation of China (grant nos. U20A2069, U21B6003, 12302389 and 12472337) and the Advanced Aero-Power Innovation Workstation (grant no. HKCX2024-01-017).

Declaration of interests. The authors report no conflict of interest.

Author ORCIDs.
Hao Yan https://orcid.org/0000-0003-1591-0050;
Chongguang Shi https://orcid.org/0000-0002-4151-3967;
Haochen Xiong https://orcid.org/0009-0001-1444-5225;
Xin Han https://orcid.org/0009-0009-4549-3164;
Yancheng You https://orcid.org/0000-0002-0463-8816.

Appendix A. RH relations for variable specific heat ratio with energy release

According to the law of conservation of mass, momentum and energy, the following equations can be obtained:

$$\rho_1 V_{1n} = \rho_2 V_{2n}, \tag{A1}$$

$$p_1 + \rho_1 {V_{1n}}^2 = p_2 + \rho_2 {V_{2n}}^2, \tag{A2}$$

$$\frac{\gamma_1}{\gamma_1 - 1}\frac{p_1}{\rho_1} + \frac{V_{1n}^2}{2} + Q_d = \frac{\gamma_2}{\gamma_2 - 1}\frac{p_2}{\rho_2} + \frac{V_{2n}^2}{2}; \tag{A3}$$

if it is assumed that

$$\frac{\rho_1}{\rho_2} = X, \tag{A4}$$

then

$$\frac{V_{2n}}{V_{1n}} = X, \quad \frac{V_{2n}^2}{V_{1n}^2} = X^2. \tag{A5a,b}$$

According to (A3), it can be derived that

$$\frac{c_{p2}T_2}{c_{p1}T_1} = 1 + \frac{V_{1n}^2}{2c_{p1}T_1}(1 - X^2) + \frac{Q_d}{c_{p1}T}, \tag{A6}$$

where c_p is the heat capacity at constant pressure. Further,

$$\frac{V_{1n}^2}{2c_{p1}T_1} = \frac{V_1^2 \sin^2\theta}{2T_1}\frac{\gamma_1 - 1}{\gamma_1 R} = \frac{V_1^2}{\gamma_1 R T_1}\frac{\gamma_1 - 1}{2}\sin^2\theta = \frac{\gamma_1 - 1}{2}M_1^2 \sin^2\theta, \tag{A7}$$

then (A7) will be

$$\frac{c_{p2}T_2}{c_{p1}T_1} = 1 + \frac{\gamma_1 - 1}{2}M_1^2 \sin^2\theta(1 - X^2) + \frac{Q_d}{c_{p1}T}, \tag{A8}$$

where

$$\frac{c_{p2}}{c_{p1}} = \frac{\gamma_2(\gamma_1 - 1)}{\gamma_1(\gamma_2 - 1)}, \tag{A9}$$

and the dimensionless energy release is

$$\tilde{Q} = \frac{Q_d}{c_{p1}T_1}. \tag{A10}$$

Thus,

$$\frac{c_{p2}T_2}{c_{p1}T_1} = \frac{\gamma_2(\gamma_1 - 1)}{\gamma_1(\gamma_2 - 1)}[1 + \gamma_1 {M_1}^2 \sin^2\theta(1 - X)]X. \tag{A11}$$

An equation appears as

$$\begin{aligned} &1 + \tilde{Q}_d + \frac{\gamma_1 - 1}{2}M_1^2\sin^2\theta - \frac{\gamma_1 - 1}{2}M_1^2\sin^2\theta X^2 \\ &\quad = \frac{\gamma_2(\gamma_1 - 1)}{\gamma_1(\gamma_2 - 1)}[X + \gamma_1 {M_1}^2\sin^2\theta X - \gamma_1 {M_1}^2\sin^2\theta X^2]. \end{aligned} \tag{A12}$$

By simplification,

$$\begin{aligned} &\left[\frac{\gamma_1 - 1}{2} + \frac{\gamma_1 - 1}{\gamma_2 - 1}\right]M_1^2\sin^2\theta X^2 - [1 + \gamma_1 {M_1}^2\sin^2\theta]\frac{\gamma_2(\gamma_1 - 1)}{\gamma_1(\gamma_2 - 1)}X + 1 + \tilde{Q}_d \\ &\quad + \frac{\gamma_1 - 1}{2}M_1^2\sin^2\theta = 0. \end{aligned} \tag{A13}$$

This is a quadratic equation in terms of X ($2aX^2 + bX + c = 0$). The following solution can be obtained:

$$X = \frac{-b \pm \sqrt{b^2 - 4ac}}{2a}, \tag{A14}$$

where

$$\left.\begin{aligned} a = \left[\frac{\gamma_1 - 1}{2} + \frac{\gamma_1 - 1}{\gamma_2 - 1}\right]M_1^2\sin^2\theta, \quad b = -[1 + \gamma_1 {M_1}^2\sin^2\theta]\frac{\gamma_2(\gamma_1 - 1)}{\gamma_1(\gamma_2 - 1)}, \\ c = 1 + \tilde{Q}_d + \frac{\gamma_1 - 1}{2}M_1^2\sin^2\theta. \end{aligned}\right\} \tag{A15a–c}$$

Thus,

$$\begin{aligned} X &= \frac{-b \pm \sqrt{b^2 - 4ac}}{2a} \\ &= \frac{(1 + \gamma_1 {M_{1n}}^2)\frac{\gamma_2(\gamma_1 - 1)}{\gamma_1(\gamma_2 - 1)} \pm \sqrt{\left[(1 + \gamma_1 {M_{1n}}^2)\frac{\gamma_2(\gamma_1 - 1)}{\gamma_1(\gamma_2 - 1)}\right]^2 - 4\left[\left(\frac{\gamma_1 - 1}{2} + \frac{\gamma_1 - 1}{\gamma_2 - 1}\right)M_{1n}^2\left(1 + \tilde{Q}_d + \frac{\gamma_1 - 1}{2}M_{1n}^2\right)\right]}}{2\left(\frac{\gamma_1 - 1}{2} + \frac{\gamma_1 - 1}{\gamma_2 - 1}\right)M_{1n}^2}. \end{aligned} \tag{A16}$$

If the specific heat ratio remains constant,

$$\gamma_2 = \gamma_1, \tag{A17}$$

then X is equal to the expression of Pratt *et al.* (1991):

$$X = \frac{(1 + \gamma_1 {M_{1n}}^2) \pm \sqrt{({M_{1n}}^2 - 1)^2 - 2(\gamma_1 + 1)M_{1n}^2\tilde{Q}_d}}{(\gamma_1 + 1)M_{1n}^2}. \tag{A18}$$

After getting the solution of X, according to (A1) and (A2), it is possible to obtain

$$\frac{p_2}{p_1} = 1 + \gamma_1 {M_1}^2 \sin^2\theta (1 - X). \tag{A19}$$

Similarly, the total post-wave parameters can be obtained.

Appendix B. The detailed derivation of the curved detonation equations

Step 1: the Euler equations are transformed from an x–y plane coordinate system to an s–n flow-coordinate system:

$$\left.\begin{aligned} \frac{\partial}{\partial s}\rho V y^j + \rho V y^j \frac{\partial \delta}{\partial n} = 0, \\ \rho V \frac{\partial V}{\partial s} + \frac{\partial p}{\partial s} = 0, \\ \rho V^2 \frac{\partial \delta}{\partial s} + \frac{\partial p}{\partial n} = 0, \\ \frac{\partial h}{\partial s} + V\frac{\partial V}{\partial s} + \frac{\partial Q_c}{\partial s} = 0, \\ \frac{\partial h}{\partial n} + V\frac{\partial V}{\partial n} + \frac{\partial Q_c}{\partial n} = 0. \end{aligned}\right\} \tag{B1}$$

Step 2: define several symbols. In curved-shock theory, the following mathematical symbols are defined to simplify the Euler equations:

$$P = \frac{1}{\rho V^2}\frac{\partial p}{\partial s}, \quad D = \frac{\partial \sigma}{\partial s}, \quad \Gamma = \frac{\omega}{V}, \quad \omega = V\frac{\partial \sigma}{\partial s} - \frac{\partial V}{\partial n}. \tag{B2a–d}$$

Since energy release is included in the Euler equations, three mathematical symbols need to be defined to emphasize the influence of energy release:

$$H = \frac{1 - \rho(\gamma - 1)Q_c/V}{1 - \rho^2(\gamma - 1)Q_c V/\gamma p}, \quad N = \frac{V - (\gamma - 1)\rho Q_c}{V - (\gamma - 1)\rho M^2 Q_c}, \quad J = \frac{V + \rho Q_c}{V - (\gamma - 1)\rho M^2 Q_c}. \tag{B3a–c}$$

It is not difficult to see that when the energy release is zero, the three coefficients H, N, J will become unity.

Step 3: simplify the Euler equations. Through the mathematical symbols defined in Step 2, the post-wave Euler equations can be simplified as follows. First, the conservation of momentum equations can be simplified to

$$\frac{1}{V}\frac{\partial V}{\partial s} = -\frac{1}{\rho V^2}\frac{\partial p}{\partial s} = -P, \quad \frac{1}{\rho V^2}\frac{\partial p}{\partial n} = -\frac{\partial \delta}{\partial s} = -D. \tag{B4a,b}$$

Next, the conservation-of-energy equations will be simplified by using this assumption and symbols:

$$\left.\begin{aligned} \frac{1}{\rho}\frac{\partial \rho}{\partial s} = HM^2 P, \\ \frac{1}{\rho}\frac{\partial \rho}{\partial n} = -M^2[ND + (\gamma - 1)J\Gamma]. \end{aligned}\right\} \tag{B5}$$

Finally, the conservation-of-mass equation can be simplified as

$$\frac{\partial \delta}{\partial n} = -(HM^2 - 1)P - j\frac{\sin\delta}{y}. \tag{B6}$$

Step 4: summary of pre- and post-wave gradients,

$$\left.\begin{aligned} \frac{\partial p_1}{\partial s} &= P_1\rho_1 V_1^2, \quad \frac{\partial p_2}{\partial s} = P_2\rho_2 V_2^2, \\ \frac{\partial p_1}{\partial n} &= -D_1\rho_1 V_1^2, \quad \frac{\partial p_2}{\partial n} = -D_2\rho_2 V_2^2, \\ \frac{\partial V_1}{\partial s} &= -P_1 V_1, \quad \frac{\partial V_2}{\partial s} = -P_2 V_2, \\ \frac{\partial V_1}{\partial n} &= V_1(D_1 - \Gamma_1), \quad \frac{\partial V_2}{\partial n} = V_2(D_2 - \Gamma_2), \\ \frac{\partial \rho_1}{\partial s} &= \rho_1 M_1^2 P_1, \quad \frac{\partial \rho_2}{\partial s} = \rho_2 M_2^2 H_2 P_2, \\ \frac{\partial \rho_1}{\partial n} &= -\rho_1 M_1^2[D_1 + (\gamma - 1)\Gamma_1], \quad \frac{\partial \rho_2}{\partial n} = -\rho_2 M_2^2[N_2 D_2 + (\gamma - 1)J_2\Gamma_2]. \end{aligned}\right\} \tag{B7}$$

Step 5: derivation of curved detonation equations. Based on the above first-order gradients, it is necessary to establish the connection between the first-order gradients based on the Rankine–Hugoniot relations between the pre- and post-wave.

Step 5.1: derivation of the mass-conservation equation,

$$\rho_1 V_1 \sin\theta = \rho_2 V_2 \sin(\theta - \delta). \tag{B8}$$

We find the partial derivatives for both sides of the equation at the same time:

$$\begin{aligned} &\frac{\partial \rho_1}{\partial \sigma} V_1 \sin\theta + \frac{\partial V_1}{\partial \sigma}\rho_1 \sin\theta + \rho_1 V_1 \cos\theta \frac{\partial \theta}{\partial \sigma} \\ &\quad = \frac{\partial \rho_2}{\partial \sigma} V_2 \sin(\theta - \delta) + \frac{\partial V_2}{\partial \sigma}\rho_2 \sin(\theta - \delta) + \rho_2 V_2 \cos(\theta - \delta)\frac{\partial(\theta - \delta)}{\partial \sigma}. \end{aligned} \tag{B9}$$

Decomposing (B9) in both the tangential and normal directions gives

$$\begin{aligned} &\left(\frac{\partial \rho_1}{\partial s}\cos\theta + \frac{\partial \rho_1}{\partial n}\sin\theta\right) V_1 \sin\theta + \left(\frac{\partial V_1}{\partial s}\cos\theta + \frac{\partial V_1}{\partial n}\sin\theta\right)\rho_1 \sin\theta \\ &\quad + \rho_1 V_1 \cos\theta \frac{\partial \theta}{\partial \sigma} = \left(\frac{\partial \rho_2}{\partial s}\cos(\theta - \delta) + \frac{\partial \rho_2}{\partial n}\sin(\theta - \delta)\right) V_2 \sin(\theta - \delta) \\ &\quad + \left(\frac{\partial V_2}{\partial s}\cos(\theta - \delta) + \frac{\partial V_2}{\partial n}\sin(\theta - \delta)\right)\rho_2 \sin(\theta - \delta) + \rho_2 V_2 \cos(\theta - \delta)\frac{\partial(\theta - \delta)}{\partial \sigma}. \end{aligned} \tag{B10}$$

We simplify (B10) using (B7), and after simplifying and rearranging, we have

$$\left.\begin{gathered} A_1P_1 + B_1D_1 + E_1\Gamma_1 = A_2P_2 + B_2D_2 + E_2\Gamma_2 + CS_a + GS_b, \\ A_1 = \sin\theta\cos\theta[2H_1M_1^2 - 2], \\ B_1 = ((1 - N_1M_1^2)\sin^2\theta - \cos^2\theta), \\ E_1 = -((\gamma - 1)J_1M_1^2 + 1)\sin^2\theta, \\ A_2 = \sin\theta\cos(\theta - \delta)[2H_2M_2^2 - 2], \\ B_2 = \sin\theta(1 - N_2M_2^2)\sin(\theta - \delta) - \dfrac{\sin\theta\cos^2(\theta - \delta)}{\sin(\theta - \delta)}, \\ E_2 = -\sin\theta\sin(\theta - \delta)((\gamma - 1)J_2M_2^2 + 1), \\ C = \dfrac{\sin\theta\cos(\theta - \delta)}{\sin(\theta - \delta)} - \cos\theta, \\ G = \dfrac{\sin\theta\cos\theta\sin\delta_1 - \sin\theta\cos(\theta - \delta)\sin\delta_2}{\cos\theta_1}. \end{gathered}\right\} \tag{B11}$$

Step 5.2: the equation of momentum conservation is derived in the same way,

$$p_1 + \rho_1V_1^2\sin^2\theta = p_2 + \rho_2V_2^2\sin^2(\theta - \delta), \tag{B12}$$

$$\begin{aligned} &\left(\frac{\partial p_1}{\partial s}\cos\theta + \frac{\partial p_1}{\partial n}\sin\theta\right) + V_1^2\sin^2\theta\left(\frac{\partial \rho_1}{\partial s}\cos\theta + \frac{\partial \rho_1}{\partial n}\sin\theta\right) \\ &\quad + 2\rho_1V_1\sin^2\theta\left(\frac{\partial V_1}{\partial s}\cos\theta + \frac{\partial V_1}{\partial n}\sin\theta\right) + 2\rho_1V_1^2\sin\theta\cos\theta\frac{\partial\theta}{\partial\sigma} \\ &= \left(\frac{\partial p_2}{\partial s}\cos(\theta - \delta) + \frac{\partial p_2}{\partial n}\sin(\theta - \delta)\right) + V_2^2\sin^2(\theta - \delta) \\ &\quad \times\left(\frac{\partial \rho_2}{\partial s}\cos(\theta - \delta) + \frac{\partial \rho_2}{\partial n}\sin(\theta - \delta)\right) \\ &\quad + 2\rho_2V_2\sin^2(\theta - \delta)\left(\frac{\partial V_2}{\partial s}\cos(\theta - \delta) + \frac{\partial V_2}{\partial n}\sin(\theta - \delta)\right) \\ &\quad + 2\rho_2V_2^2\sin(\theta - \delta)\cos(\theta - \delta)\frac{\partial(\theta - \delta)}{\partial\sigma}, \end{aligned} \tag{B13}$$

$$\begin{aligned} &(P_1\rho_1V_1^2\cos\theta - D_1\rho_1V_1^2\sin\theta) + V_1^2\sin^2\theta(\rho_1M_1^2H_1P_1\cos\theta \\ &\quad - \rho_1M_1^2[N_1D_1 + (\gamma - 1)J_1\Gamma_1]\sin\theta) \\ &\quad + 2\rho_1V_1\sin^2\theta(-P_1V_1\cos\theta + V_1(D_1 - \Gamma_1)\sin\theta) \\ &\quad + 2\rho_1V_1^2\sin\theta\cos\theta\left[S_a + (H_1M_1^2 - 1)\sin\theta P_1 - \cos\theta D_1 + \frac{\sin\theta\sin\delta_1}{y}\right] \end{aligned}$$

$$
\begin{aligned}
&= (P_2\rho_2V_2^2\cos(\theta-\delta) - D_2\rho_2V_2^2\sin(\theta-\delta))\\
&\quad + V_2^2\sin^2(\theta-\delta)(\rho_2H_2M_2^2P_2\cos(\theta-\delta)\\
&\quad - \rho_2M_2^2[N_2D_2 + (\gamma-1)J_2\Gamma_2]\sin(\theta-\delta))\\
&\quad + 2\rho_2V_2\sin^2(\theta-\delta)(-P_2V_2\cos(\theta-\delta) + V_2(D_2-\Gamma_2)\sin(\theta-\delta))\\
&\quad + 2\rho_2V_2^2\sin(\theta-\delta)\cos(\theta-\delta)\left[S_a + (H_2M_2^2-1)\sin(\theta-\delta)P_2\right.\\
&\quad \left. - \cos(\theta-\delta)D_2 + \frac{\sin(\theta-\delta)\sin\delta_2}{y}\right].
\end{aligned}
\tag{B14}
$$

The same terms are combined, so the equation of the second curved detonation is

$$
\left.
\begin{aligned}
A_1'P_1 + B_1'D_1 + E_1'\Gamma_1 &= A_2'P_2 + B_2'D_2 + E_2'\Gamma_2 + C'S_a + G'S_b,\\
A_1' &= \cos\theta(1 + 3H_1M_1^2\sin^2\theta - 4\sin^2\theta),\\
B_1' &= \sin\theta(-1 - N_1M_1^2\sin^2\theta + 2\sin^2\theta - 2\cos^2\theta),\\
E_1' &= \sin^3\theta(-(\gamma-1)J_1M_1^2 - 2),\\
A_2' &= \frac{\sin\theta\cos\theta}{\sin(\theta-\delta)} + \sin\theta\cos\theta(3H_2M_2^2 - 4)\sin(\theta-\delta),\\
B_2' &= \frac{\sin\theta\cos\theta(-1 - N_2M_2^2\sin^2(\theta-\delta) + 2\sin^2(\theta-\delta) - 2\cos^2(\theta-\delta))}{\cos(\theta-\delta)},\\
E_2' &= -\frac{\sin\theta\cos\theta\sin^2(\theta-\delta)((\gamma-1)J_2M_2^2 + 2)}{\cos(\theta-\delta)},\\
C' &= 0,\\
G' &= \frac{2\sin^2\theta\cos\theta\sin\delta_1 - 2\sin\theta\cos\theta\sin(\theta-\delta)\sin\delta_2}{\cos\theta_1}.
\end{aligned}
\right\}
\tag{B15}
$$

Step 5.3: the equation of tangential velocity is

$$
V_1\cos\theta = V_2\cos(\theta-\delta),
\tag{B16}
$$

$$
V_1\frac{\partial\cos\theta}{\partial\sigma} + \cos\theta\frac{\partial V_1}{\partial\sigma} = V_2\frac{\partial\cos(\theta-\delta)}{\partial\sigma} + \cos(\theta-\delta)\frac{\partial V_2}{\partial\sigma},
\tag{B17}
$$

$$
\begin{aligned}
&\sin\theta\frac{\partial\theta}{\partial\sigma} - \cos\theta\left[\frac{1}{V_1}\cos\theta\frac{\partial V_1}{\partial s} + \frac{1}{V_1}\sin\theta\frac{\partial V_1}{\partial n}\right]\\
&= \frac{V_2}{V_1}\left[\sin(\theta-\delta)\frac{\partial(\theta-\delta)}{\partial\sigma}\right]\\
&\quad - \cos(\theta-\delta)\frac{V_2}{V_1}\left[\cos(\theta-\delta)\frac{1}{V_2}\frac{\partial V_2}{\partial s} + \sin(\theta-\delta)\frac{1}{V_2}\frac{\partial V_2}{\partial n}\right],
\end{aligned}
\tag{B18}
$$

where

$$\frac{V_2}{V_1} = \frac{\cos\theta}{\cos(\theta-\delta)}, \tag{B19}$$

$$\begin{aligned}
&\sin\theta\left[S_a + (H_1M_1^2 - 1)\sin\theta P_1 - \cos\theta D_1 + \frac{\sin\theta\sin\delta_1}{y}\right] \\
&\quad + \cos^2\theta P_1 - \cos\theta\sin\theta(D_1 - \Gamma_1) \\
&= \cos\theta\tan(\theta-\delta)\left[S_a + (H_2M_2^2 - 1)\sin(\theta-\delta)P_2\right. \\
&\quad \left. - \cos(\theta-\delta)D_2 + \frac{\sin(\theta-\delta)\sin\delta_2}{y}\right] \\
&\quad - \cos\theta[-\cos(\theta-\delta)P_2 + \sin(\theta-\delta)(D_2 - \Gamma_2)].
\end{aligned} \tag{B20}$$

After combination and collation, a third curved detonation equation can be obtained

$$\left.\begin{aligned}
A_1''P_1 + B_1''D_1 + E_1''\Gamma_1 &= A_2''P_2 + B_2''D_2 + E_2''\Gamma_2 + C''S_a + G''S_b, \\
A_1'' &= (H_1M_1^2 - 1)\sin\theta\tan\theta + \cos\theta, \\
E_1'' &= -2\sin\theta, \\
B_1'' &= \sin\theta, \\
A_2'' &= (H_2M_2^2 - 1)\sin(\theta-\delta)\tan(\theta-\delta) + \cos(\theta-\delta), \\
B_2'' &= -2\sin(\theta-\delta), \\
E_2'' &= \sin(\theta-\delta), \\
C'' &= \tan(\theta-\delta) - \tan\theta, \\
G'' &= \tan(\theta-\delta)\sin(\theta-\delta)\sin\delta_2 - \sin\theta\tan\theta\sin\delta_1.
\end{aligned}\right\} \tag{B21}$$

Step 6: complete curved-detonation equations

$$\left.\begin{aligned}
A_1P_1 + B_1D_1 + E_1\Gamma_1 &= A_2P_2 + B_2D_2 + E_2\Gamma_2 + CS_a + GS_b, \\
A_1'P_1 + B_1'D_1 + E_1'\Gamma_1 &= A_2'P_2 + B_2'D_2 + E_2'\Gamma_2 + C'S_a + G'S_b, \\
A_1''P_1 + B_1''D_1 + E_1''\Gamma_1 &= A_2''P_2 + B_2''D_2 + E_2''\Gamma_2 + C''S_a + G''S_b.
\end{aligned}\right\} \tag{B22}$$

Appendix C. The derivation of curved detonation equations with chemical reaction

The derivation process of the CEDC is similar to CDE in Appendix B, with the main difference lying in the governing equations of chemical reaction added to the Euler equations, and the pre-wave and post-wave relationships. The single-step Arrhenius equation is used to simulate chemical reaction processes and the ZND structure is shown in figure 32. Here is the specific derivation.

Step 1: Euler equations with chemical reaction.

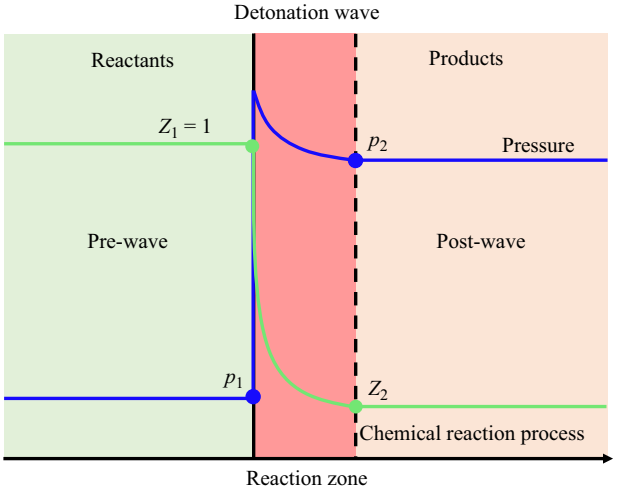

Figure 32. Schematic of the ZND structure of the detonation wave.

Due to the presence of a chemical reaction, the two-dimensional Euler equations in the Cartesian coordinate can be written in the following form:

$$\frac{\partial}{\partial x}\begin{bmatrix} \rho V_x \\ \rho V_x^2 + p \\ \rho V_x V_y \\ (\rho e + p) V_x \\ \rho Z V_x \end{bmatrix} + \frac{\partial}{\partial y}\begin{bmatrix} \rho V_y \\ \rho V_y^2 + p \\ \rho V_x V_y \\ (\rho e + p) V_y \\ \rho Z V_y \end{bmatrix} = \begin{bmatrix} 0 \\ 0 \\ 0 \\ 0 \\ \bar{\sigma} \end{bmatrix}, \tag{C1}$$

where V_x and V_y are the velocity components in the x and y direction, respectively; e is the specific energy. The chemical reaction is modelled with a single-step Arrhenius equation, where the source function $\bar{\sigma}$ can be defined as

$$\bar{\sigma} = -\rho k Z \exp(-E_a \rho / p). \tag{C2}$$

Among them, the conservation of mass, momentum and energy equations remain unchanged. Here, focus on handling the chemical reaction item. In the streamline-coordinates,

$$\frac{\partial}{\partial s}\rho Z V + \rho Z V \frac{\partial \delta}{\partial n} = \bar{\sigma}. \tag{C3}$$

Further simplification yields

$$\frac{\partial Z}{\partial s} = \frac{\bar{\sigma} - Z V \dfrac{\partial \rho}{\partial s} - \rho Z \dfrac{\partial V}{\partial s} - \rho Z V \dfrac{\partial \delta}{\partial n}}{\rho V}. \tag{C4}$$

Step 2: define the standard process gradient variable.

If the process gradient variable κ is defined as

$$\kappa = \frac{\partial Z}{\partial n} - Z\frac{\partial \bar{\sigma}}{\partial s}, \tag{C5}$$

then, the standard process gradient variable Ω can be defined as

$$\Omega = \frac{\kappa}{Z}. \tag{C6}$$

With this definition, it is possible to derive

$$\frac{\partial Z}{\partial n} = (\Omega - D)Z. \tag{C7}$$

Up to here, the gradient variables of chemical reaction process in both s and n directions (C4) and (C7) are expressed properly. The next step is to solve the relationship between different gradient variables based on the above definitions in combination with Euler equations.

Step 3: Euler equations in the s and n streamline coordinates.

Similar to the previous derivation, the Euler equations in the streamline coordinates can be derived from (C1):

$$\left.\begin{gathered}\frac{\partial}{\partial s}\rho V y^j + \rho V y^j \frac{\partial \delta}{\partial n} = 0, \\ \left.\begin{gathered}\rho V\frac{\partial V}{\partial s} + \frac{\partial p}{\partial s} = 0 \\ \rho V^2\frac{\partial \delta}{\partial s} + \frac{\partial p}{\partial n} = 0\end{gathered}\right\}, \\ \left.\begin{gathered}\frac{\partial h}{\partial s} + V\frac{\partial V}{\partial s} + \frac{\partial Q}{\partial s} = 0 \\ \frac{\partial h}{\partial n} + V\frac{\partial V}{\partial n} + \frac{\partial Q}{\partial n} = 0\end{gathered}\right\}, \\ \frac{\partial}{\partial s}\rho Z V + \rho Z V\frac{\partial \delta}{\partial n} = \bar{\sigma},\end{gathered}\right\} \tag{C8}$$

where Q is the energy release in the Euler equation. The derivation of the momentum and vorticity equations is consistent with the previous ones, but due to the involvement of chemical reactions, the new form of mass equation need to be re-derived:

$$\left.\begin{gathered}\frac{\partial}{\partial s}\rho V + \rho V\frac{\partial \delta}{\partial n} = 0, \\ \frac{\partial \delta}{\partial n} = -\frac{1}{V}\frac{\partial V}{\partial s} - \frac{1}{\rho}\frac{\partial \rho}{\partial s}.\end{gathered}\right\} \tag{C9}$$

Taking the definition of the pressure gradient and simplifying leads to

$$\frac{\partial \delta}{\partial n} = P - \frac{1}{\rho}\frac{\partial \rho}{\partial s}. \tag{C10}$$

Thus, the partial derivative of Z in the s-direction can be simplified from (C4):

$$\frac{\partial Z}{\partial s} = \frac{\bar{\sigma}}{\rho V}. \tag{C11}$$

Combined with the derivation of the CDE, the following relational equations for the gradient variable can be obtained:

$$\left.\begin{aligned} \frac{\partial \delta}{\partial s} &= D, \quad \frac{\partial \delta}{\partial n} = P - \frac{1}{\rho}\frac{\partial \rho}{\partial s}, \\ \frac{\partial p}{\partial s} &= \rho V^2 P, \quad \frac{\partial p}{\partial n} = -\rho V^2 D, \\ \frac{\partial V}{\partial s} &= -PV, \quad \frac{\partial V}{\partial n} = V(D - \Gamma), \\ \frac{\partial Z}{\partial s} &= \frac{\bar{\sigma}}{\rho V}, \quad \frac{\partial Z}{\partial n} = (\Omega - D)Z. \end{aligned}\right\} \tag{C12}$$

By observing (C12), it can be realized that the gradient variables of the density are now missing. An additional definition is given based on the research results (Turns 2013) in this paper since it is taken into account that the energy release can be related to parameters such as the flow rate, chemical reaction process and fuel itself:

$$Q = \rho V q Z, \tag{C13}$$

where q is the energy released by a complete chemical reaction per unit mass flow rate. With the above relationship of variables, the density gradients can further be solved by solving the energy conservation equations:

$$\left.\begin{aligned} \frac{\gamma}{\gamma - 1}\frac{\partial}{\partial s}\frac{p}{\rho} + V\frac{\partial V}{\partial s} + \frac{\partial}{\partial s}\rho V q Z = 0 \\ \frac{\gamma}{\gamma - 1}\frac{\partial}{\partial n}\frac{p}{\rho} + V\frac{\partial V}{\partial n} + \frac{\partial}{\partial n}\rho V q Z = 0 \end{aligned}\right\}, \tag{C14}$$

after simplification:

$$\frac{\partial \rho}{\partial s} = \frac{\rho M^2 P[\rho q(1 - Z)(\gamma - 1)/V - 1] + (\gamma - 1)\rho q \bar{\sigma} M^2 / V^2}{(\gamma - 1)\rho^2 V q(1 - Z)/\gamma p - 1}, \tag{C15}$$

$$\frac{\partial \rho}{\partial n} = \frac{\begin{array}{c}[V - (1 - Z)(\gamma - 1)\rho q - (\gamma - 1)\rho q Z]M^2 \rho D \\ + [V + \rho q(1 - Z)]M^2 \rho(\gamma - 1)\Gamma + (\gamma - 1)\rho^2 M^2 q Z \Omega\end{array}}{(\gamma - 1)M^2 q(1 - Z)\rho - V}. \tag{C16}$$

If the coefficient variables are defined as

$$H_z = \frac{\rho q(1 - Z)(\gamma - 1)/V - 1}{(\gamma - 1)\rho^2 V q(1 - Z)/\gamma p - 1}, \tag{C17}$$

$$H_c = \frac{q\bar{\sigma}(\gamma - 1)/V^2}{(\gamma - 1)\rho^2 V q(1 - Z)/\gamma p - 1}, \tag{C18}$$

$$N_z = -\frac{V - (1 - Z)(\gamma - 1)\rho q - (\gamma - 1)\rho q Z}{(\gamma - 1)M^2 q(1 - Z)\rho - V}, \tag{C19}$$

$$J_z = -\frac{V + \rho q(1-Z)}{(\gamma-1)M^2 q(1-Z)\rho - V}, \tag{C20}$$

$$R_z = -\frac{\rho q Z}{(\gamma-1)M^2 q(1-Z)\rho - V}, \tag{C21}$$

then the density gradients can be expressed as

$$\left.\begin{aligned} \frac{\partial \rho}{\partial s} &= \rho M^2 (H_z P + H_c), \\ \frac{\partial \rho}{\partial n} &= -\rho M^2 [N_z D + J_z(\gamma-1)\Gamma + (\gamma-1)R_z \Omega]. \end{aligned}\right\} \tag{C22}$$

In addition, the partial derivation of curvature (S_a) is

$$\left.\begin{aligned} S_a &= \frac{\partial \theta}{\partial \sigma} + \frac{\partial \delta_1}{\partial \sigma}, \\ \frac{\partial \delta}{\partial \sigma} &= D_1 \cos\theta - \left\{ [(H_{z1} M_1^2 - 1)P_1 - M_1^2 H_{c1}] - j\frac{\sin\delta_1}{y} \right\} \sin\theta, \\ \frac{\partial \theta}{\partial \sigma} &= S_a + (H_{z1} M_1^2 - 1)\sin\theta P_1 - D_1 \cos\theta - M_1^2 H_{c1} \sin\theta - \frac{\sin\delta_1}{y}\sin\theta. \end{aligned}\right\} \tag{C23}$$

The partial derivation of curvature (S_b) is

$$\left.\begin{aligned} \frac{1}{y} &= -\frac{S_b}{\cos\theta_1}, \\ \frac{\partial \theta}{\partial \sigma} &= S_a + (H_{z1} M_1^2 - 1)\sin\theta P_1 - D_1 \cos\theta - M_1^2 H_{c1} \sin\theta \\ &\quad - \frac{\sin\theta \sin\delta_1}{\cos\theta_1} S_b, \\ \frac{\partial(\theta - \delta)}{\partial \sigma} &= S_a + (H_{z2} M_2^2 - 1)\sin(\theta-\delta) P_2 - D_2 \cos(\theta - \delta) \\ &\quad - M_2^2 H_{c2} \sin(\theta - \delta) - \frac{\sin(\theta-\delta)\sin\delta_2}{\cos\theta_1} S_b. \end{aligned}\right\} \tag{C24}$$

In summary, all the variables can be displayed:

$$\frac{\partial V}{\partial s} = -PV, \quad \frac{\partial V}{\partial n} = V(D - \Gamma), \tag{C25a,b}$$

$$\frac{\partial \rho}{\partial s} = \rho M^2 (H_z P + H_c), \quad \frac{\partial \rho}{\partial n} = -\rho M^2 [N_z D + J_z(\gamma-1)\Gamma + (\gamma-1)R_z \Omega], \tag{C26a,b}$$

$$\frac{\partial p}{\partial s} = \rho V^2 P, \quad \frac{\partial p}{\partial n} = -\rho V^2 D, \tag{C27a,b}$$

$$\frac{\partial Z}{\partial s} = \frac{\bar{\sigma}}{\rho V}, \quad \frac{\partial Z}{\partial n} = (\Omega - D)Z, \tag{C28a,b}$$

$$\frac{\partial \delta}{\partial s} = D, \quad \frac{\partial \delta}{\partial n} = -(H_z M^2 - 1)P - M^2 H_c. \tag{C29a,b}$$

Since the above variables are derived based on the Euler equations, the pre-wave and post-wave will be of the same form if both are in chemical equilibrium. Otherwise, the two forms do not agree, and a distinction should be made between pre-wave and post-wave. However, for convenience, a uniform form is used here, except that $Z = 1$ is taken for the pre-wave and Z for the post-wave is taken, with the specified value based on the chemical reactions.

Step 4: derivation of pre-wave and post-wave relations.

With the above gradient variables, the following derivation can be made for the pre- and post-wave relationships in detonation.

Step 4.1: mass conservation relationship.

$$\rho_1 V_1 \sin\theta = \rho_2 V_2 \sin(\theta - \delta). \tag{C30}$$

According to the above relationship (consistent with (B8)) and the law of vector decomposition, it can be obtained by simplification similar to (B9)–(B11):

$$\left.\begin{gathered}
A_1 P_1 + B_1 D_1 + E_1 \Gamma_1 + I_1 \Omega_1 = A_2 P_2 + B_2 D_2 + E_2 \Gamma_2 + I_2 \Omega_2 + C S_a + G S_b, \\
A_1 = 2\sin\theta\cos\theta(H_{z1} M_1^2 - 1), \\
B_1 = (1 - M_1^2 N_{z1})\sin^2\theta - \cos^2\theta, \\
E_1 = -\sin^2\theta(M_1^2 J_{z1}(\gamma - 1) + 1), \\
I_1 = -M_1^2 \sin^2\theta(\gamma - 1) R_{z1}, \\
A_2 = 2\sin\theta\cos(\theta - \delta)(H_{z2} M_2^2 - 1), \\
B_2 = (1 - M_2^2 N_{z2})\sin(\theta - \delta)\sin\theta - \frac{\cos^2(\theta - \delta)}{\sin(\theta - \delta)}\sin\theta, \\
E_2 = -\sin(\theta - \delta)\sin\theta(M_2^2 J_{z2}(\gamma - 1) + 1), \\
I_2 = -M_2^2 \sin(\theta - \delta)\sin\theta(\gamma - 1) R_{z2}, \\
C = \frac{\sin\theta\cos(\theta - \delta)}{\sin(\theta - \delta)} - \cos\theta, \\
G = \frac{\sin\theta\cos\theta\sin\delta_1 - \sin\theta\cos(\theta - \delta)\sin\delta_2}{\cos\theta_1}.
\end{gathered}\right\} \tag{C31}$$

Step 4.2: momentum conservation relationship.

$$p_1 + \rho_1 {V_1}^2 \sin^2\theta = p_2 + \rho_2 {V_2}^2 \sin^2(\theta - \delta). \tag{C32}$$

By similarity, the second equation can be obtained:

$$\left.\begin{gathered}
A_1'P_1 + B_1'D_1 + E_1'\Gamma_1 + I_1'\Omega_1 = A_2'P_2 + B_2'D_2 + E_2'\Gamma_2 + I_2'\Omega_2 + C'S_a + G'S_b + \Delta, \\
A_1' = \cos\theta(1 + 3\sin^2\theta M_1^2 H_{z1} - 4\sin^2\theta), \\
B_1' = \sin\theta(-1 - \sin^2\theta M_1^2 N_{z1} + 2\sin^2\theta - 2\cos^2\theta), \\
E_1' = -\sin^3\theta(M_1^2 J_{z1}(\gamma - 1) + 2), \\
I_1' = -M_1^2\sin^3\theta(\gamma - 1)R_{z1}, \\
A_2' = \frac{\sin\theta\cos\theta}{\sin(\theta - \delta)} + \sin\theta\cos\theta\sin(\theta - \delta)(3M_2^2 H_{z2} - 4), \\
B_2' = \frac{\sin\theta\cos\theta(-1 - \sin^2(\theta - \delta)M_2^2 N_{z2}) + 2\sin^2(\theta - \delta) - 2\cos(\theta - \delta)}{\cos(\theta - \delta)}, \\
E_2' = -\frac{\sin\theta\cos\theta\sin^2(\theta - \delta)}{\cos(\theta - \delta)}(M_2^2 J_{z2}(\gamma - 1) + 2), \\
I_2' = -\frac{\sin\theta\cos\theta\sin^2(\theta - \delta)}{\cos(\theta - \delta)}M_2^2(\gamma - 1)R_{z2}, \\
C' = 0 \\
G' = \frac{\sin\theta\cos\theta\sin\delta_1 - \sin\theta\cos(\theta - \delta)\sin\delta_2}{\cos\theta_1}, \\
\Delta = -\sin\theta\cos\theta M_2^2\sin(\theta - \delta)H_{c2} + H_{c1}M_1^2\sin^2\theta\cos\theta.
\end{gathered}\right\} \tag{C33}$$

Step 4.3: relationship of vorticity.

$$V_1\cos\theta = V_2\cos(\theta - \delta). \tag{C34}$$

Thus,

$$\left.\begin{gathered}
A_1''P_1 + B_1''D_1 + E_1''\Gamma_1 = A_2''P_2 + B_2''D_2 + E_2''\Gamma_2 + C''S_a + G''S_b, \\
A_1'' = \sin\theta(H_{z1}M_1^2 - 1)\sin\theta + \cos\theta\cos\theta, \\
B_1'' = -2\sin\theta\cos\theta, \\
E_1'' = \sin\theta\cos\theta, \\
A_2'' = (H_{z2}M_2^2 - 1)\sin(\theta - \delta)\frac{\cos\theta\sin(\theta - \delta)}{\cos(\theta - \delta)} + \cos\theta\cos(\theta - \delta), \\
B_2'' = -2\cos\theta\sin(\theta - \delta), \\
E_2'' = -\sin(\theta - \delta)\cos\theta, \\
C'' = \frac{\cos\theta\sin(\theta - \delta)}{\cos(\theta - \delta)} - \sin\theta, \\
G'' = \sin\theta\frac{\sin\theta\sin\delta_1}{\cos\theta_1} - \frac{\sin(\theta - \delta)\sin\delta_2}{\cos\theta_1}\frac{\cos\theta\sin(\theta - \delta)}{\cos(\theta - \delta)}.
\end{gathered}\right\} \tag{C35}$$

Step 4.4: chemical reaction term.

$$\rho_1 V_1 \sin\theta Z_1 - \bar{\sigma}_1 = \rho_2 V_2 \sin(\theta - \delta) Z_2 - \bar{\sigma}_2. \tag{C36}$$

In a similar way, it can be obtained after simplification:

$$\left.\begin{aligned}
A_1''' P_1 + B_1''' D_1 + E_1''' \Gamma_1 + I_1''' \Omega_1 &= A_2''' P_2 + B_2''' D_2 + E_2''' \Gamma_2 + I_2''' \Omega_2 \\
&\quad + C''' S_a + G''' S_b + \Delta', \\
A_1''' &= \rho_1 M_1^2 H_{z1} \cos\theta C_{n1} - V_1 \cos\theta \rho_1 \sin\theta Z_1 + (H_{z1} M_1^2 - 1) \sin\theta \rho_1 V_1 \cos\theta Z_1 \\
&\quad - C_{n3} \rho_1 V_1^2 \cos\theta, \\
B_1''' &= \{-\rho_1 M_1^2 N_{z1} \sin\theta C_{n1} + V_1 \sin\theta \rho_1 \sin\theta Z_1 - \cos\theta \rho_1 V_1 \cos\theta Z_1 \\
&\quad - Z_1 \sin\theta [\rho_1 V_1 \sin\theta - \rho_1 k \exp(-Ea \rho_1 / p_1)] + C_{n3} \rho_1 V_1^2 \sin\theta\}, \\
E_1''' &= -\rho_1 M_1^2 J_{z1} (\gamma - 1) \sin\theta C_{n1} - V_1 \sin\theta \rho_1 \sin\theta Z_1, \\
I_1''' &= \{-\rho_1 M_1^2 (\gamma - 1) R_{z1} \sin\theta C_{n1} + Z_1 \sin\theta [\rho_1 V_1 \sin\theta - \rho_1 k \exp(-Ea \rho_1 / p_1)]\}, \\
A_2''' &= \rho_2 M_2^2 H_{z2} \cos(\theta - \delta) C_{n2} - V_2 \cos(\theta - \delta) \rho_2 \sin(\theta - \delta) Z_2 \\
&\quad + (H_{z2} M_2^2 - 1) \sin(\theta - \delta) \rho_2 V_2 \cos(\theta - \delta) Z_2 - \rho_2 V_2^2 \cos(\theta - \delta) C_{n4}, \\
B_2''' &= \{-\rho_2 M_2^2 N_{z2} \sin(\theta - \delta) C_{n2} + V_2 \sin(\theta - \delta) \rho_2 \sin(\theta - \delta) Z_2 \\
&\quad - \cos(\theta - \delta) \rho_2 V_2 \cos(\theta - \delta) Z_2 - Z_2 \sin(\theta - \delta) [\rho_2 V_2 \sin(\theta - \delta) \\
&\quad - \rho_2 k \exp(-Ea \rho_2 / p_2)] + \rho_2 V_2^2 \sin(\theta - \delta) C_{n4}\}, \\
E_2''' &= -\rho_2 M_2^2 N_{z2} J_{z2} (\gamma - 1) \sin(\theta - \delta) C_{n2} - V_2 \sin(\theta - \delta) \rho_2 \sin(\theta - \delta) Z_2, \\
I_2''' &= \{-\rho_2 M_2^2 (\gamma - 1) R_{z2} \sin(\theta - \delta) C_{n2} + Z_2 \sin(\theta - \delta) [\rho_2 V_2 \sin(\theta - \delta) \\
&\quad - \rho_2 k \exp(-Ea \rho_2 / p_2)]\}, \\
C''' &= \rho_2 V_2 \cos(\theta - \delta) Z_2 - \rho_1 V_1 \cos\theta Z_1, \\
G''' &= \frac{\sin\theta \sin\delta_1}{\cos\theta_1} \rho_1 V_1 \cos\theta Z_1 - \frac{\sin(\theta - \delta) \sin\delta_2}{\cos\theta_1} \rho_2 V_2 \cos(\theta - \delta) Z_2, \\
\Delta' &= H_{c2} [\rho_2 M_2^2 \cos(\theta - \delta) C_{n2} - M_2^2 \sin(\theta - \delta) \rho_2 V_2 \cos(\theta - \delta) Z_2] \\
&\quad + \frac{\sigma_2}{\rho_2 V_2} \cos(\theta - \delta) [\rho_2 V_2 \sin(\theta - \delta) - \rho_2 k \exp(-Ea \rho_2 / p_2)] \\
&\quad - H_{c1} [\rho_1 M_1^2 \cos\theta C_{n1} - M_1^2 \sin\theta \rho_1 V_1 \cos\theta Z_1] \\
&\quad - \frac{\sigma_1}{\rho_1 V_1} \cos\theta [\rho_1 V_1 \sin\theta - \rho_1 k \exp(-Ea \rho_1 / p_1)],
\end{aligned}\right\} \tag{C37}$$

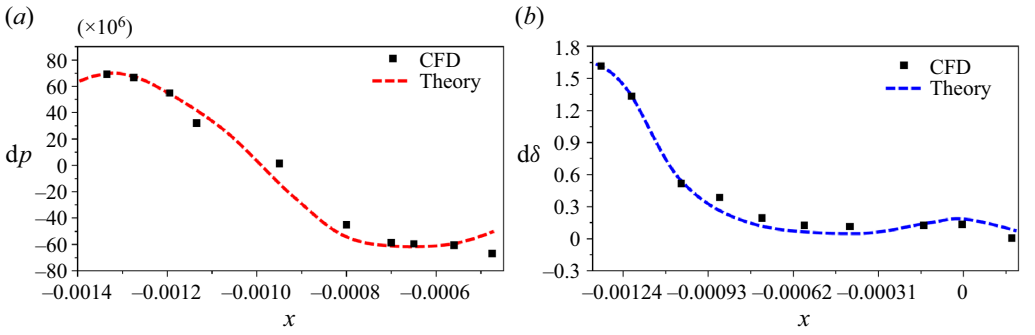

Figure 33. Comparison of the post-wave gradient parameters: (*a*) pressure gradient; (*b*) streamline curvature. The dashed lines of red and blue colour are the results calculated from the CDEC, the black squares are the simulation results.

where

$$\left.\begin{aligned} C_{n1} &= \left[V_1 \sin\theta Z_1 - kZ_1 \exp(-Ea\rho_1/p_1) + Ea\rho_1 kZ_1 \exp(-Ea\rho_1/p_1)\frac{1}{p_1}\right], \\ C_{n2} &= \left[V_2 \sin(\theta-\delta) Z_2 - kZ_2 \exp(-Ea\rho_2/p_2) + Ea\rho_2 kZ_2 \exp(-Ea\rho_2/p_2)\frac{1}{p_2}\right], \\ C_{n3} &= Ea\rho_1 kZ_1 \exp(-Ea\rho_1/p_1)\frac{\rho_1}{p_1^2}, \\ C_{n4} &= Ea\rho_2 kZ_2 \exp(-Ea\rho_2/p_2)\frac{\rho_2}{p_2^2}. \end{aligned}\right\} \tag{C38}$$

Step 5: the complete equations of curved detonation equations with chemical reaction.

Compared with the CDE, there is not only one new equation added, but two additional variables (chemical process gradients: Ω_1, Ω_2) are added to each equation. The CDEC is expected to describe the gradient variables of detonation more accurately and comprehensively.

$$\left.\begin{aligned} A_1P_1 + B_1D_1 + E_1\Gamma_1 + I_1\Omega_1 &= A_2P_2 + B_2D_2 + E_2\Gamma_2 \\ &\quad + I_2\Omega_2 + CS_a + GS_b, \\ A_1'P_1 + B_1'D_1 + E_1'\Gamma_1 + I_1'\Omega_1 &= A_2'P_2 + B_2'D_2 + E_2'\Gamma_2 + I_2'\Omega_2 \\ &\quad + C'S_a + G'S_b + \Delta, \\ A_1''P_1 + B_1''D_1 + E_1''\Gamma_1 &= A_2''P_2 + B_2''D_2 + E_2''\Gamma_2 + C''S_a + G''S_b, \\ A_1'''P_1 + B_1'''D_1 + E_1'''\Gamma_1 + I_1'''\Omega_1 &= A_2'''P_2 + B_2'''D_2 + E_2'''\Gamma_2 + I_2'''\Omega_2 \\ &\quad + C'''S_a + G'''S_b + \Delta'. \end{aligned}\right\} \tag{C39}$$

To verify the effectiveness of CDEC, the evidence is shown in figure 33. For the same numerical simulation results in figures 21 and 24, the curves from CDEC are represented by dashed lines. It is reasonable that the calculated results are closer due to the addition of chemical reactions.

Appendix D. Influence coefficient format of curved detonation equations

For the purpose of obtaining the equations in a form including influence coefficients, we first need to eliminate the post-wave vorticity. To achieve this, the following mathematical definitions are required:

$$\left.\begin{gathered} L = A_1P_1 + B_1D_1 + E_1\Gamma_1, \quad L' = A_1'P_1 + B_1'D_1 + E_1'\Gamma_1, \\ L'' = A_1''P_1 + B_1''D_1 + E_1''\Gamma_1, \\ S_{ab} = CS_a + GS_b, \quad S_{ab}' = C'S_a + G'S_b, \quad S_{ab}'' = C''S_a + G''S_b, \\ AE_1 = E_2A_2' - E_2'A_2, \quad AE_2 = E_2A_2'' - E_2''A_2, \quad BE_1 = E_2B_2' - E_2'B_2, \\ BE_2 = E_2B_2'' - E_2''B_2. \end{gathered}\right\} \tag{D1}$$

With these definitions, we can obtain the equations with no vorticity:

$$\left.\begin{aligned} L'E_2 - LE_2' &= AE_1P_2 + BE_1D_2 + E_2S_{ab}' - E_2'S_{ab}, \\ L''E_2 - LE_2'' &= AE_2P_2 + BE_2D_2 + E_2S_{ab}'' - E_2''S_{ab}. \end{aligned}\right\} \tag{D2}$$

Next, we eliminate the streamline curvature so we can get an explicit expression of the post-wave pressure gradient:

$$P_2 = \frac{BE_2(L'E_2 - LE_2' - E_2S_{ab}' + E_2'S_{ab}) - BE_1(L''E_2 - LE_2'' + E_2S_{ab}'' - E_2''S_{ab})}{AE_2BE_1 - AE_1BE_2}. \tag{D3}$$

Similarly, we can eliminate the pressure gradient. We can then get the explicit expression of the streamline curvature:

$$D_2 = \frac{AE_2(L'E_2 - LE_2' - E_2S_{ab}' + E_2'S_{ab}) - AE_1(L''E_2 - LE_2'' + E_2S_{ab}'' - E_2''S_{ab})}{AE_2BE_1 - AE_1BE_2}. \tag{D4}$$

After determining these two gradients, we can express the vorticity with the pressure gradient and streamline curvature:

$$\Gamma_2 = \frac{L - A_2P_2 - B_2D_2 - S_{ab}}{E_2}. \tag{D5}$$

Finally, the pressure gradient, streamline curvature and vorticity of the post-wave can be written in the influence-coefficient form:

$$\left.\begin{aligned} P_2 &= J_pP_1 + J_dD_1 + J_g\Gamma_1 + J_aS_a + J_bS_b, \\ D_2 &= K_pP_1 + K_dD_1 + K_g\Gamma_1 + K_aS_a + K_bS_b, \\ \Gamma_2 &= F_pP_1 + F_dD_1 + F_g\Gamma_1 + F_aS_a + F_bS_b, \end{aligned}\right\} \tag{D6}$$

in which the influence coefficients are

$$\left.\begin{aligned} J_p &= (BE_2E_2A_1' - BE_2E_2'A - BE_1E_2A_1'' + BE_1E_2''A_1)/ABE,\\ J_d &= (BE_2E_2B_1' - BE_2E_2'B_1 - BE_1E_2B_1'' + BE_1E_2''B_1)/ABE,\\ J_g &= (BE_2E_2E_1' - BE_2E_2'E_1 - BE_1E_2E_1'' + BE_1E_2''E_1)/ABE,\\ J_a &= (-BE_2C'E_2 + BE_2CE_2' - BE_1E_2C'' + BE_1E_2''C)/ABE,\\ J_b &= (-BE_2G'E_2 + BE_2GE_2' - BE_1E_2G'' + BE_1E_2''G)/ABE. \end{aligned}\right\} \tag{D7}$$

$$\left.\begin{aligned} K_p &= (AE_2E_2A_1' - AE_2E_2'A - AE_1E_2A_1'' + AE_1E_2''A_1)/ABE,\\ K_d &= (AE_2E_2B_1' - AE_2E_2'B_1 - AE_1E_2B_1'' + AE_1E_2''B_1)/ABE,\\ K_g &= (AE_2E_2E_1' - AE_2E_2'E_1 - AE_1E_2E_1'' + AE_1E_2''E_1)/ABE,\\ K_a &= (-AE_2C'E_2 + AE_2CE_2' - AE_1E_2C'' + AE_1E_2''C)/ABE,\\ K_b &= (-AE_2G'E_2 + AE_2GE_2' - AE_1E_2G'' + AE_1E_2''G)/ABE. \end{aligned}\right\} \tag{D8}$$

$$\left.\begin{aligned} F_p &= (A_1 - A_2J_p - B_2K_p)/E_2,\\ F_d &= (B_1 - A_2J_d - B_2K_d)/E_2,\\ F_g &= (E_1 - A_2J_g - B_2K_g)/E_2,\\ F_a &= -(A_2J_a + B_2K_a + C)/E_2,\\ F_b &= -(A_2J_b + B_2K_b + G)/E_2. \end{aligned}\right\} \tag{D9}$$

In the above, $ABE = AE_2BE_1 - AE_1BE_2$. These influence coefficients directly show that the post-wave first-order gradients are affected by the pre-wave flow conditions and the curvatures, which is helpful to better understand and analyse the detonation. The coefficients give the effects of pre-wave flow and curvatures on the post-wave in a mathematical form, turning the previous qualitative understanding into a quantified expression. For example, prior to this research, it was only possible to guess that an increase in curvature would lead to a larger post-wave first-order gradient, and there was no way to know exactly what would be the effect.

Appendix E. Grid resolution verification

Boundary conditions and geometric parameters for numerical simulations are given in figure 34. To verify the credibility of the numerical simulation results for pressure and deflection angle capture, three different grid schemes are shown in table 5. Take the coarse grid scheme as an example, where 250 grids were laid out over a horizontal distance of 4 mm and 225 grids over a vertical distance of 7.5 mm. Each grid has dimensions of 0.016 and 0.03 mm horizontally and vertically, and has 7.5 grids per reaction zone which is increased to 15 and 30 for the medium and fine grid schemes, respectively. According to the research by Choi, Ma & Yang (2008), to accurately capture the pressure of the detonation flow field, in the general case, 5 grid points per reaction zone are selected, which can be increased to 12–15 grid points in highly unstable detonations. In this sense, the medium grid strategy (15 grids) is sufficient to capture the accurate pressure in this paper. To further compare the computational performance of the three grids, the corresponding flow field calculation results are shown in figure 35.

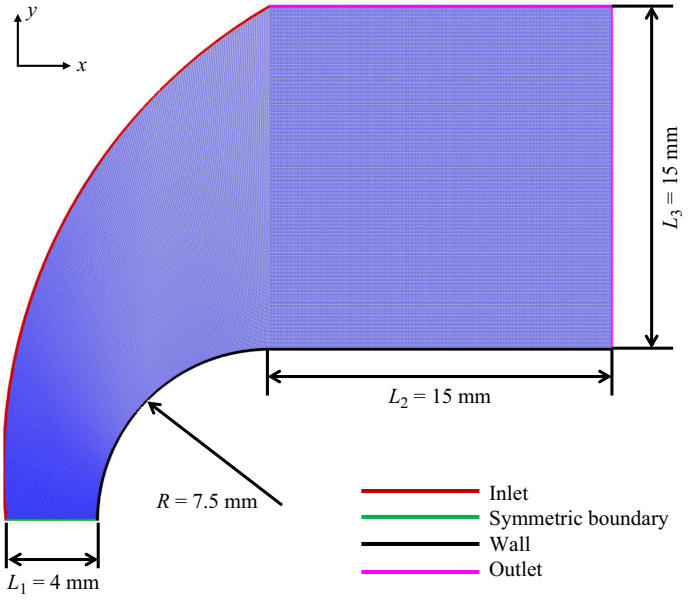

Figure 34. Boundary conditions and geometric parameters for numerical simulations.

Grid size	Size in x-direction (mm)	Size in y-direction (mm)	Grids per reaction zone
Coarse	$4/250 = 0.016$	$7.5/225 = 0.03$	7.5
Medium	$4/500 = 0.008$	$7.5/450 = 0.016$	15
Fine	$4/1000 = 0.004$	$7.5/900 = 0.008$	30

Table 5. Grid schemes at different levels.

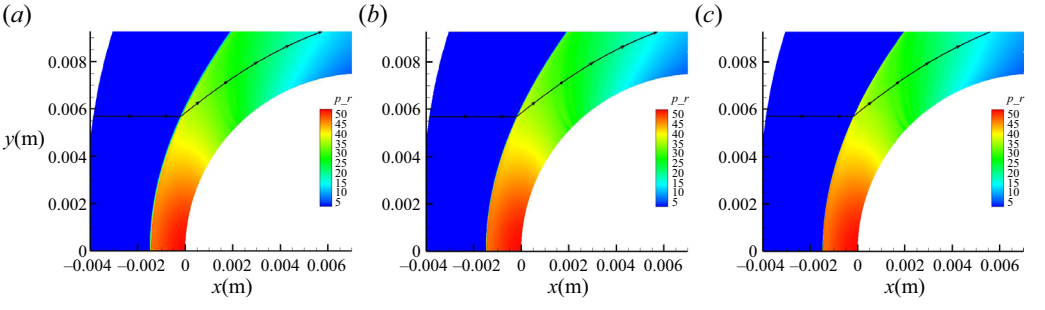

Figure 35. Pressure contours of the detonation flow field for different grid sizes: (*a*) coarse grid; (*b*) medium grid; (*c*) fine grid.

Macroscopically speaking, the flow fields of the three grid schemes have great similarity. Further, the aerodynamic parameters on the three streamlines at the same location are plotted in figure 36.

In figure 36(*a*), the variation of pressure and mass fraction of hydrogen on the three streamlines shows the successful initiation of detonation, and the general pattern is similar for all three. To quantitatively compare the specific differences, the pressure at the peak

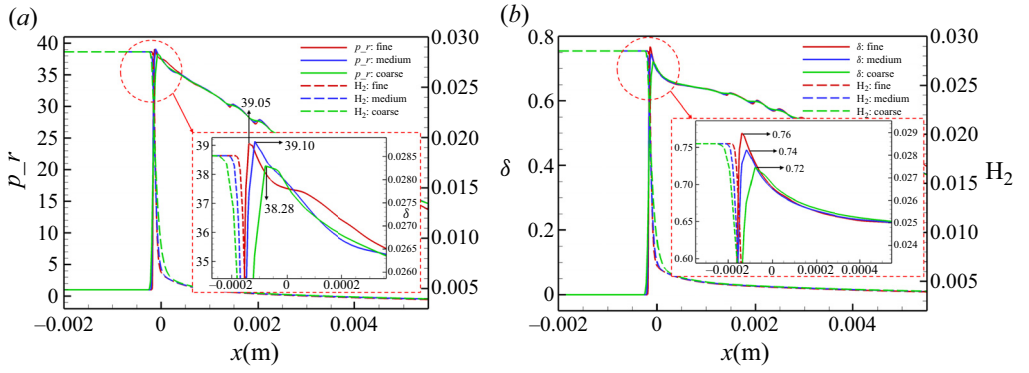

Figure 36. Aerodynamic parameters on streamlines under different grid sizes: (*a*) pressure and mass fraction of hydrogen; (*b*) deflection angle and mass fraction of hydrogen.

Grid size	Pressure ratio	Deflection angle (radian)
Coarse	38.28	0.72
Medium	39.10	0.74
Fine	39.05	0.76
Error	(0.13 %, 1.9 %)	(2.6 %, 5.2 %)

Table 6. Comparison of calculation results and errors for different grid sizes.

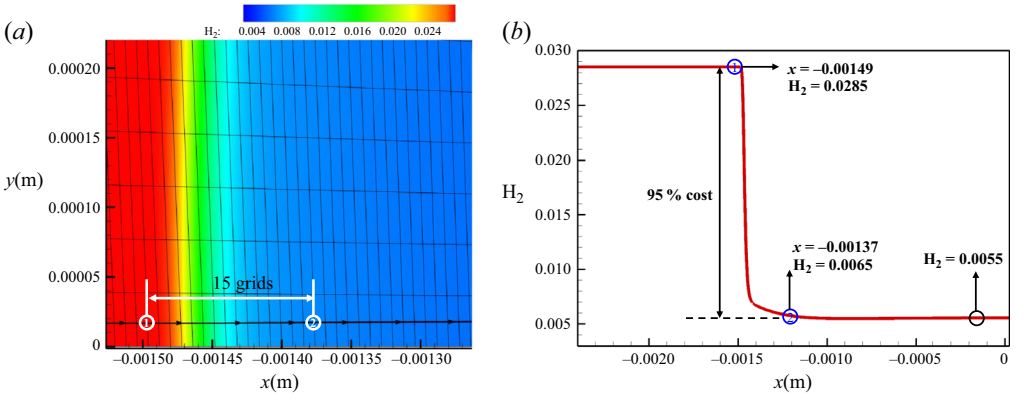

Figure 37. Grid situation per reaction zone length: (*a*) hydrogen mass fraction contour at the lower boundary and its grid situation; (*b*) hydrogen mass fraction on the streamline.

was picked up and displayed in table 6. Similarly, the same operation was performed for the deflection angle. According to table 6, it is known that if the fine grid is used as a standard, the maximum error of the medium grid for both pressure and airflow deflection angle does not exceed 3 %, which is acceptable for the study of this paper. Furthermore, to get a clearer view of the number of grids within a reaction zone under medium grid scheme, figure 37 is plotted. This is a locally enlarged view around the low wall where the detonation wave angle is nearly 90°. According to figure 37(*b*), it is known that the hydrogen mass fraction at point 1 is 0.285 and at the far end is 0.0055. Therefore, when the hydrogen mass decreases by 95 % to 0.0065, it can be considered as the post-wave state

of the detonation, which is the position of point 2. In figure 37(*a*), marking the position of both points 1, 2 and counting the grid number between them, it can be known that there are 15 grid points per reaction zone, which is in agreement with the pre-given results in table 5. In summary, given that the medium grid scheme captures accurate pressure and meets the requirement of grid number per reaction zone, it was chosen in this paper.

References

Abel, F.A. 1874 X. Contributions to the history of explosive agents.–Second memoir. *Phil. Trans. R. Soc. Lond.* **164**, 337–395.

Bdzil, J.B. & Short, M. 2016 Theory of mach reflection of detonation at glancing incidence. *J. Fluid Mech.* **811**, 269–314.

Berthelot, M. & Vieille, P. 1881 On the velocity of propagation of explosive processes in gases. *C. R. Hebd. Sceances Acad. Sci.* **93** (2), 18–21.

Chapman, D.L. 1899 VI. On the rate of explosion in gases. *Lond. Edinb. Dubl. Phil. Mag. J. Sci.* **47** (284), 90–104.

Chatelier, L., *et al.* 1885 Recherches sur la combustion des mélanges gazeux explosifs. *J. Phys. Théor. Appl.* **4** (1), 59–84.

Cheng, W., Luo, X. & Dongen, M.V. 2010 On condensation-induced waves. *J. Fluid Mech.* **651**, 145–164.

Choi, J.-Y., Kim, D.-W., Jeung, I.-S., Ma, F. & Yang, V. 2007 Cell-like structure of unstable oblique detonation wave from high-resolution numerical simulation. *Proc. Combust. Inst.* **31** (2), 2473–2480.

Choi, J.Y., Ma, F.H. & Yang, V. 2008 Some numerical issues on simulation of detonation cell structures. *Combust. Explosion Shock Waves* **44** (5), 560–578.

Crocco, L. 1937 Singolarita della corrente gassosa iperacustica nell'interno di una prora adiedro. *L'Aerotecnica* **17** (6), 519–534.

Denisov, Y.N. 1959 Pulsating and spinning detonation of gaseous mixtures in tubes. *Dokl. Akad. Nauk SSSR* **125**, 110–113.

Doring, W. 1943 Detonation waves. *Ann. Phys.* **43**, 421–436.

Dou, H.-S., Tsai, H.M., Khoo, B.C. & Qiu, J. 2008 Simulations of detonation wave propagation in rectangular ducts using a three-dimensional weno scheme. *Combust. Flame* **154** (4), 644–659.

Emanuel, G. 2018 Analytical extension of curved shock theory. *Shock Waves* **28** (2), 417–425.

Emanuel, G. & Mölder, S. 2022 Three-dimensional curved shock theory. *Shock Waves* **32** (2), 129–146.

Eto, K., Tsuboi, N. & Hayashi, A.K. 2005 Numerical study on three-dimensional CJ detonation waves: detailed propagating mechanism and existence of oh radical. *Proc. Combust. Inst.* **30** (2), 1907–1913.

Han, W., Wang, C. & Law, C.K. 2019 Three-dimensional simulation of oblique detonation waves attached to cone. *Phys. Rev. Fluids* **4** (5), 053201.

Hornung, H.G. 1998 Gradients at a curved shock in reacting flow. *Shock Waves* **8** (1), 11–21.

Jachimowski, C.J. 1988 An analytical study of the hydrogen-air reaction mechanism with application to scramjet combustion. *NASA Tech. Paper* 2791.

Jouguet, E. 1904 Remarques sur la propagation des percussions dans les gaz. *C. R. Acad. Sci. Paris* **138**, 1685–1688.

Jouguet, E. 1905 On the propagation of chemical reactions in gases. *J. Math. Pures Appl.* **1** (386), 347–425.

Jouguet, É. 1916 *Mécanique des Explosifs: étude de Dynamique Chimique*. Octave Doin.

Kaneshige, M. & Shepherd, J.E. 1997 Detonation database. *Tech. Rep.* California Institute of Technology.

Kasahara, J., Arai, T., Chiba, S., Takazawa, K., Yu, T. & Matsuo, A. 2002 Criticality for stabilized oblique detonation waves around spherical bodies in acetylene/oxygen/krypton mixtures. *Proc. Combust. Inst.* **29** (2), 2817–2824.

Klein, R. & Stewart, D.S. 1993 The relation between curvature, rate state-dependence, and detonation velocity. *SIAM J. Appl. Maths* **53** (5), 1401–1435.

Lee, J.H.S. 2008 *The Detonation Phenomenon*. Cambridge University Press.

Lehr, H.F. 1972 Experiments on shock-induced combustion. *Astronaut. Acta* **17**, 589–597.

Lobb, R.K. 1964 Experimental measurement of shock detachment distance on spheres fired in air at hypervelocities - sciencedirect. *Agardograph* **68**, 519–527.

Maeda, S., Kasahara, J. & Matsuo, A. 2012 Unsteady propagation process of oblique detonation waves initiated by hypersonic spherical projectiles. *Trans. JSASS Aerospace Tech. Japan* **10** (ists28), Pe_1–Pe_6.

Maeda, S., Sumiya, S., Kasahara, J. & Matsuo, A. 2013 Initiation and sustaining mechanisms of stabilized oblique detonation waves around projectiles. *Proc. Combust. Inst.* **34** (2), 1973–1980.

MENEES, G.P., ADELMAN, H.G., CAMBIER, J.-L. & BOWLES, J.V. 1992 Wave combustors for trans-atmospheric vehicles. *J. Propul. Power* **8** (3), 709–713.

MÖLDER, S. 2016 Curved shock theory. *Shock Waves* **26** (4), 337–353.

MÖLDER, S. 2017*a* Flow behind concave shock waves. *Shock Waves* **27** (5), 721–730.

MÖLDER, S. 2017*b* Reflection of curved shock waves. *Shock Waves* **27** (5), 699–720.

MÖLDER, S. 2017*c* Shock detachment from curved wedges. *Shock Waves* **27** (5), 731–745.

PARK, C. 1985 Convergence of computation of chemical reacting flows. *Prog. Astronaut. Aeronaut.* **103**, 478–513.

PRATT, D.T., HUMPHREY, J.W. & GLENN, D.E. 1991 Morphology of standing oblique detonation waves. *J. Propul. Power* **7** (5), 837–845.

SHARPE, G.J. 2007*a* The effect of curvature on pathological detonations. *Combust. Flame* **123** (1–2), 68–81.

SHARPE, G.J. 2007*b* The structure of planar and curved detonation waves with reversible reactions. *Phys. Fluids* **12** (11), 3007–3020.

SHI, C., HAN, W., DEITERDING, R., ZHU, C. & YOU, Y. 2020 Second-order curved shock theory. *J. Fluid Mech.* **891**, A21.

SHI, C., ZHU, C., YOU, Y. & ZHU, G. 2021 Method of curved-shock characteristics with application to inverse design of supersonic flowfields. *J. Fluid Mech.* **920**, A36.

TAKI, S. & FUJIWARA, T. 1978 Numerical analysis of two-dimensional nonsteady detonations. *AIAA J.* **16** (1), 73–77.

TENG, H.H. & JIANG, Z.L. 2012 On the transition pattern of the oblique detonation structure. *J. Fluid Mech.* **713**, 659–669.

THOMAS, T.Y. 1947 On curved shock waves. *Stud. Appl. Maths* **26** (1–4), 62–68.

TURNS, S.R. 2013 *An Introduction into Combustion Concepts and Applications*. McGraw-Hill Education.

VERREAULT, J. 2011 Initiation of gaseous detonation by conical projectiles. PhD thesis, McGill University.

VERREAULT, J., HIGGINS, A.J. & STOWE, R.A. 2012 Formation and structure of steady oblique and conical detonation waves. *AIAA J.* **50** (8), 1766–1772.

VON NEUMAN, J. 1942 Theory of detonation waves. *Tech. Rep.* Institute for Advanced Study.

WATT, S.D. & SHARPE, G.J. 2004 One-dimensional linear stability of curved detonations. *Proc. R. Soc. Lond.* A **460** (2049), 2551–2568.

WEN, C.Y., MASSIMI, H.S. & SHEN, H. 2017 Extension of ce/se method to non-equilibrium dissociating flows. *J. Comput. Phys.* **356**, 240–260.

XIANG, G., ZHANG, Y., TU, Q., GAO, Y., HUANG, X. & PENG, T. 2022 The initiation characteristics of oblique detonation waves induced by a curved surface. *Aerosp. Sci. Technol.* **128**, 107743.

YAN, H., HAN, X., XIONG, H., SHI, C. & YOU, Y. 2024 Curved detonation and its reflections. *J. Fluid Mech.* **984**, A11.

YANG, P., NG, H.D., TENG, H. & JIANG, Z. 2017 Initiation structure of oblique detonation waves behind conical shocks. *Phys. Fluids* **29** (8), 086104.

YAO, J. & STEWART, D.S. 1995 On the normal detonation shock velocity-curvature relationship for materials with large activation energy. *Combust. Flame* **100** (4), 519–528.

ZEL'DOVICH, Y.B. 1940 On the theory of the propagation of detonation in gaseous systems. *Zh. Eksp. Teor. Fiz.* **10**, 542–568.

ZHANG, Z., WEN, C., ZHANG, W., LIU, Y. & JIANG, Z. 2022 A theoretical method for solving shock relations coupled with chemical equilibrium and its applications. *Chin. J. Aeronaut.* **35** (6), 47–62.